Boston University

OpenBU **http://open.bu.edu**

Theses & Dissertations Boston University Theses & Dissertations

2018

Solutions to linear problems in aberrated optical systems

https://hdl.handle.net/2144/31761

Boston University

BOSTON UNIVERSITY

GRADUATE SCHOOL OF ARTS AND SCIENCES

Dissertation

SOLUTIONS TO LINEAR PROBLEMS IN ABERRATED OPTICAL SYSTEMS

by

WILLIAM J. SHAIN

B.A., Boston University, 2011

Submitted in partial fulfillment of the
requirements for the degree of
Doctor of Philosophy
2018

© 2018 by
WILLIAM J. SHAIN
All rights reserved

Approved by

First Reader

Bennett B. Goldberg, PhD
Professor of Physics

Second Reader

Tom Bifano, PhD
Professor of Mechanical Engineering

Third Reader

Jerome Mertz, PhD
Professor of Physics and Biomedical Engineering

ויאמר אלקים יהי אור ויהי אור

... Let there be Light ...

Genesis 1:3 בראשית א:ג

Acknowledgments

This thesis is the culmination of my work as a graduate student in physics, indeed of my entire scientific career thus far. Thank G-d, it is finally complete. There are a great many people who have helped me along this path, and to whom I owe immense gratitude, and I most certainly will not be able to express that gratitude sufficiently, nor even to all those who deserve it. So if you don't find your name here with sufficient praise (or at all), please let me know and I will be more than happy to thank you and celebrate with you in person.

In that context, I would like to thank my extensive and wonderful group of friends and mentors, from my childhood throughout my final years here at Boston University. There are many times I have relied on you for intellectual, emotional, and moral support, without which this work would not have happened. I would like to thank the many teachers I have had, and the many classmates, and the many students as well, in physics, mathematics, and all the other varied subjects I have had throughout my career.

A special thanks to the various agencies that have funded this project over the years: the Aramco services company, the NSF, and the Boston University Photonics Center.

In particular, I would like to thank the members of the Precision Engineering Research Laboratory at Boston University who helped at various points in this thesis: Chris Stockbridge, Hari Paudel, Jiang Li, and Nic Vickers, all of whom directly contributed to this thesis in both thought and deed. I would like to thank as well Prof. Anne Sentenac and Prof. Lei Tian for their insightful and enlightening discussions about the mathematics of imaging, and Prof. Shyam Erramilli for his assistance in both theoretical and practical matters of optics. I would like to thank Prof. Pankaj

Mehta, Prof. Claudio Chamon, and Prof. David Campbell for teaching me a great deal of theoretical physics, and for serving on my committee (often on short notice).

A great deal of thanks goes to my four graduate advisors: to Prof. Steve Ahlen, for teaching me to recover from my mistakes; to Prof. Bennett Goldberg, for teaching me how to learn about the world and how to teach it as well; to Prof. Jerome Mertz, for teaching me how to come up with a worthwhile project, and to Prof. Tom Bifano, for teaching me how to actually finish it. Every one of my advisors has shaped my capabilities and my career in far more ways than this, and I am immensely fortunate to have worked with each of them.

I would also like to thank my family: my many siblings and siblings-in-law (present and future), my parents and in-laws for supporting me and encouraging me to pursue this path and to love it; to find all these wonderful teachers, and to ask of them good questions. I am immensely grateful to my wonderful children for ensuring that I get up in the morning, and to my wonderful wife for ensuring that I do get some much-needed rest at night.

Finally, I would like to thank you for taking the time to read this and making it part of your accumulated knowledge, and by extension making it a small step towards a better understanding of our universe.

William J Shain
Boston University
Physics Department

SOLUTIONS TO LINEAR PROBLEMS IN ABERRATED OPTICAL SYSTEMS

WILLIAM J. SHAIN

Boston University, Graduate School of Arts and Sciences, 2018

Major Professor: Bennett B. Goldberg, PhD
Professor of Physics

ABSTRACT

Linear problems are possibly the kindest problems in physics and mathematics. Given sufficient information, the linear equations describing such problems are intrinsically solvable. The solution can be written as a vector having undergone a linear transformation in a vector space; extracting the solution is simply a matter of inverting the transformation. In an ideal optical system, the problem of extracting the object under investigation would be well defined, and the solution trivial to implement. However, real optical systems are all aberrated in some way, and these aberrations obfuscate the information, scrambling it and rendering it inextricable. The process of detangling the object from the aberrated system is no longer a trivial problem or even a uniquely solvable one, and represents one of the great challenges in optics today. This thesis provides a review of the theory behind optical microscopy in the presence of absent information, an architecture for the modern physical and computational methods used to solve the linear inversion problem, and three distinct application spaces of relevance. I hope you find it useful.

Contents

1 Introduction to Optical Microscopy **1**

1.1 Origins of the Classical Microscope 1

1.2 Modern Adaptive Optics 4

2 Basic Linearity in Optics **8**

2.1 Fluid Flow in Porous Rock 8

2.2 Super-penetrative Multi-Photon Microscopy 10

2.3 Multi-Point Optimization 13

3 Deconvolution Algorithms and Applications **17**

3.1 Dynamic Volumetric Imaging 17

3.1.1 Extended Depth-of-Field with Axial Scanning Microscope . . . 18

3.2 Open-Loop Deconvolution 20

3.2.1 Deconvolving Extended Depth-of-Field Images 22

3.3 Axial Localization with Modulated Illumination 24

3.3.1 Experimental Validation 26

3.3.2 Discriminating Neurons with Depth Information 31

3.4 Blind Deconvolution 34

3.4.1 Dual fluorescence-absorption deconvolution 35

4 Compressive Linear Systems with Constraints **39**

4.1 Matched-Filter Compressive Imaging (MFCI) Flow Cytometry 39

4.2 Implementation of MFCI Flow Cytometer 40

4.3 Linear Inversion through Machine Learning 45

5 Conclusions 48

5.1 A General Linear Microscopy Framework 48

A Derivation of the Classical Microscope Propagator 50

A.1 The Origin of Plane Waves 50

A.1.1 Plane Wave Decomposition 50

A.1.2 Making an Image 52

A.1.3 The Classic Microscope 53

B Optical Characterization of Porous Rock 57

B.1 Transport Mean-Free-Path 57

B.2 Sample Bandwidth and Diffusion Coefficient 59

C Image Analysis in Low SNR environments 63

C.1 Partitioning by Local Maxima 63

C.2 Primary Image Metrics 65

D Derivation of Deconvolution Approximations 68

D.1 Derivation of Modulated OTF 68

References 72

Curriculum Vitae 79

List of Figures

1·1 Implementing an SLM corrects for aberrations in an aberrated microscope 5

1·2 Deformable mirrors with different surface structures generate phase shifts in incoming light. Phase shifts are proportional to the local deflection of the DM surface, set by electrostatically controlled pistons. 6

2·1 Schematic representation of light passing through a scattering medium, resulting in poissonian intensity fluctuations in the transmitted light (a form of speckle) 8

2·2 Deformable Mirror (DM) used to refocus light through scattering media to a single point 12

2·3 Aberration correction with an S-MPM Microscope 13

2·4 Left: 200μm x 200μm 2-Photon image of natural rock fluorescence from Arab-D rock surface , with 1μm fluorescent bead layer 100μm below (not visible). Right: Fluorescent beads before and after applying S-MPM correction. 13

2·5 Diagramical representation of MPO solution 14

2·6 Stitch imaging of 1μm beads. Field-of-view is 10μm x 10μm. (a) without correction, (b) single optimized sweep image (c) step scan is shown, (d) local maxima, (e-f) manual stitching of five images. . . . 15

3·1 Schematic of EDOF Microscope. Vertical dashed line indicates location of intermediate image plane. 20

3·2 Classic vs. EDOF microscope imaging of 1μm diameter fluorescent beads embedded in PDMS. Images taken with 20× 0.5NA objective; EDOF=70μm with 26 DM frames. Beads that are defocused in the standard image (a) reappear in the EDOF image (b). Normalized axial PSFs for classic and EDOF microscope demonstrate significand increase of the DOF under focal scanning (c). Lateral PSFs for classic and EDOF microscope are shown in (d), illustrating that while EDOF maintains the lateral resolution as defined by the FWHM it increases the surrounding intensity as well. Scale bar is 25m. 21

3·3 (a) A classical microscope image of tissue marked with fluorescent highlighter shows intricate detail in a small in-focus region and a blurred object elsewhere. (b) An EDOF image uniformly blurs the object, occluding it throughout the FOV. (c) EDOF with deconvolution removes the blur across the image, restoring full resolution to the parts of the objcet within the scan range ($D = 70\mu m$); parts of the object outside the scan range remain blurred, as the EDOF model for the OTF does not take them into account. 23

3·4 EOTF (red) and MOTF (black) curves for a focal scan range of 60μm, as a function of spatial frequency normalized to the diffraction limit. Example regularization parameters (blue, purple) are shown for reference. 26

3·5 Verification of axial localization with an isolated 1μm bead (inset). Scale-bar is 5μm. Intensity of the bead as a function of stage position before (solid red) and after (solid black) deconvolution illustrates the range of the extended DOF of about 60μm. Axial localization of the bead before deconvolution (red) shows good agreement with the nominal stage position (dotted black) over the extended DOF (slope $\approx$ 0.8, $r^2 = 0.996$). Axial localization with a single (blue) and double (black) parameter deconvolution shows improved axial accuracy (slope $\approx$ 0.9, $r^2 = 0.997$). 27

3·6 Verification of axial localization with an extended cluster of 1μm beads (inset). Scale-bar is 5μm. Axial localization of the cluster before (red) deconvolution shows linearity but poor accuracy in estimating the axial position within the DOF, systematically underestimating deviations from $Z = 0$ (slope $\approx$ 0.4, $r^2 = 0.983$). After applying deconvolution (blue) with a single regularization parameter the accuracy improves significantly (slope $\approx$ 0.8, $r^2 = 0.998$). Two-parameter deconvolution (black) provides even higher accuracy (slope $\approx$ 0.9, r^2 = 0.999) which extends even beyond the focal scan range of 60μm. . . 29

3·7 MI-EDOF images of 4μm beads embedded in PDMS acquired with fluorescence (top left) and darkfield (top right) imaging modes. Axial displacement from nominal focus is represented by the color axis (in units of microns); scale bar is 50μm. Comparison of the axial positions obtained in fluorescence and darkfield modes is also shown (bottom), yielding a linear fit of slope 1.02, and offset 3.2μm. 30

3·8 Cylindrospermum algae acquired with ALMI in darkfield mode using a 20× 0.5NA Olympus objective (left). From the modulated-illumination image, two algae strands appear to overlap at two distinct points (A and B). Plots of the recorded axial location of each strand (top right) near point B reveal sharp variations that converge to a common axial location, indicative of an incorrect apparent co-localization of the strands. The convergence at point A occurs at much more slowly, suggesting the two strands are in fact co-localized at that point. This is verified by an x-z projection obtained from an image stack, where we confirm that the strands are axially co-located point A but axially separated at point B. The different behaviors of axial plots about these points suggests that with prior information about the sample (such as continuity constraints), correct axial information can be inferred even in non-co-localized cases. 32

3·9 a) In-vivo ALMI data from GCaMP-labeled neurons in a mouse striatum (three frames are shown from a video). Distinct neurons are observed (blue, green) in the indicated ROI that laterally overlap (purple); scalebar is 50μm. b,c) Intensity and depth variations are monitored simultaneously, facilitating the discrimination of neuronal activity. d1-3) ALMI video frames show neurons firing either individually or together; scalebars are 20μm. e1-2) Intensity and depth of neurons firing almost simultaneously. f1-3) ALMI video frames show near-simultaneous firing of neurons; scalebars are 20μm 33

3·10 Time projection of mouse motor cortex taken with EDOF microscope; FOV ≈ 250 μm. a) raw EDOF images, b) open-loop deconvolution, c,d) fluorescence and absorbing structures using DFA deconvolution. . 37

4·1 Schematic of MFCI Flow Cytometer 41

4·2 Normalized images of beads, yeast, and bascillus cerus taken in image and pupil planes. A net intensity drop is consistantly seen in all pupil plane images where the ballistic light is reduced due to scattering. For the 4μm bead (left), this light is scattered into a ring about the ballistic component; for the yeast bacteria (center), the light is scattered farther out due to the finer structure of the bacteria cell; for the bascillus cerus bacteria (right), there is increased scattering along the thin axis of the bacteria relative to the long axis, due to the asymmetry of the bacteria geometry. 42

4·3 Example of Bead flowing past detector for a specific DM pattern. As the bead passes the FOV, the intensity in each channel is deflected (either increasing or decreasing) as light is scattered away from or into the corresponding spatial frequencies 43

4·4 Average output signals $< \delta I_c >$ of 4μm diameter beads and yeast bacteria flowing past MFCI flow cytometer. Filter applied to separate signals is shown in figure 4·3. Clear separation between the beads and the yeast signals are visible in each of the four channels. 44

4·5 Linearity of LED illumination vs. Laser Illumination: groups of 2μm beads placed in the FOV and imaged with both a laser and an LED source. Intensity in each channel is recorded, after subtracting a line of best-fit as a linear assumption. For laser illumination (blue circles) in each channel, the intensity varied wildly depending on the number of beads; whereas with LED illumination (red x's), the intensity was relatively constant even with significant changes in particle count. . . 46

A·1 Propagation of light through a homogeneous medium. 51

A·2 Propagation of light through a thin film for an arbitrary wave plate and for a quadratic phase 52

A·3 Fourier-conjugate nature of positions and angles between one focal plane of a lens and the other. 54

A·4 Classical Microscope System 56

B·1 Diagram of light travelling through a scattering medium. Initially the light retains its directionality, but by l^* (dotted line) the light is now diffusing evenly throughout the sample. 58

B·2 a) Diagram of laser pulse incident on scattering media. The ballistic light exits as if there were no scattering, retaining the pulse shape. The scattered light exits after the ballistic light, and spreads significantly in time. b) Diagram of sample bandwidth. Broad pulse corresponds to a beam of finite bandwidth. For a finite bandwidth Δ_l incident on a scattering media, the spectrum is divided into blocks of width $\Delta\nu_s$ which remain coherent. The above spectrum, for example, is broken into approximately four distinct modes. 61

B·3 Schematic of setup used to measure the sample bandwidth Δ_s. An SLD was directed onto a diffraction grating and spatially filtered with a tunable slit; from there it was recombined and redirected to the sample, and the transmitted light imaged on the camera. SLD: Superluminescent diode, PBS: polarizing beam splitter, ND: neutral density filter, QWP: quarter wave plate, DM: deformable mirror, L: lens, M: mirror 62

C·1 Threshold and cluster method used to identify 1μm diameter beads in a 20μm x20μm image. Each pixel in the initial image (a) is defined as signal or background, creating a binary image (b). Adjacent signal pixels are combined to form a single structure, such as a bead (c). However, the algorithm may misidentify a chain of beads as a single structure (d) or isolate a few pixels (e). 64

C·2 Use of partitioning to identify beads. Initial image (a) is broken into local regions with local maxima (b). By taking a local measure of the intensity and plotting a histogram of the regions (c), we see regions naturally separate into background and signal. This lets us identify and quantify the bead intensities and geometries 65

C·3 Output of analysis program applied to 20μm x 20μm image of 1μm diameter beads (no scattering). The structures creating signal are identified, and the relevant image metrics and parameters are recorded. Scale bar: 1μm 66

List of Abbreviations

ALMI	....	Axial Localization with Modulated Illumination
AO	....	Adaptive Optics
BMC	....	Boston Micromachines Corporation
CSF	....	Coherent Spread Function
CTF	....	Coherent Transfer Function
DFA	....	Dual Fluorescence Absorption
DM	....	Deformable Mirror
DOF	....	Depth-of-Field
EDOF	....	Extended Depth-of-Field
EOTF	....	Extended Optical Transfer Function
EPSF	....	Extended Point-Spread Function
FOV	....	Field of View
FWHM	....	Full-Width at Half Maximum
GPSF	....	Gaussian Point-Spread Function
MFCI	....	Matched-Filter Compressed Imaging
ML	....	Machine Learning
MOTF	....	Modulated Optical Transfer Function
MPO	....	Multi-Point Optimization
NA	....	Numerical Aperature
ND	....	Neutral Density Filter
OTF	....	Optical Transfer Function
PBS:	....	Polarizing Beam Splitter
PSF	....	Point Spread Function
QWP	....	Quarter Wave Plate
ROI	....	Region of Interest
SLD	....	Super-Luminescent Diode
SLM	....	Spatial Light Modulator
S-MPM	....	Superpenetrative Multi-photon Microscopy
TTP-DM	....	Tip-Tilt-Piston Deformable Mirror

Chapter 1

Introduction to Optical Microscopy

1.1 Origins of the Classical Microscope

For over a century, the core of any study in electromagentic phenomena has been Maxwell's equations (Jackson, 1999):

$$\begin{aligned} \nabla \cdot \vec{D} &= \rho_f \\ \nabla \cdot \vec{B} &= 0 \\ \nabla \times \vec{E} &= -\frac{\partial \vec{B}}{\partial t} \\ \nabla \times \vec{H} &= \vec{J}_f + \frac{\partial \vec{D}}{\partial t} \end{aligned} \tag{1.1}$$

These equations describe the interaction between all electromagnetically charged objects, as mediated by the electromagnetic fields. When the charges are separated by a neutral medium with a linear refractive index n_r, equations 1.1 decouple into separate vector equations for the electric and magnetic fields:

$$\begin{aligned} \left(\frac{n_r}{c}\frac{\partial^2}{\partial t^2} - \nabla^2\right)\vec{E} &= 0 \\ \left(\frac{n_r}{c}\frac{\partial^2}{\partial t^2} - \nabla^2\right)\vec{B} &= 0 \end{aligned} \tag{1.2}$$

The solutions to these equations are the radiative (and decaying) complex fields we call light. The key feature to the wave formulation given by equations 1.2 is that the propagation of the fields is linear. The form of the linear propagation operator suggests the appropriate bases eigenfunctions are complex exponentials. The propogation in a given spatial direction $\hat{k}$ can be defined by decomposing the fields into oscillating functions of uniform lateral intensity, called plane waves (Jackson, 1999):

$$\begin{aligned} \vec{E}_{k_z}(\vec{r},t) &= E_0 e^{i2\pi(\vec{k}\cdot\vec{r}-wt)}\hat{\epsilon}_1 \\ \vec{B}_{k_z}(\vec{r},t) &= \frac{1}{c}E_0 e^{i2\pi(\vec{k}\cdot\vec{r}-wt)}\hat{\epsilon}_2 \\ \hat{k} &= \frac{\vec{k}}{|\vec{k}|} = \hat{\epsilon}_1 \times \hat{\epsilon}_2 \end{aligned} \tag{1.3}$$

As can be verified by plugging equations 1.3 into equations 1.2 to get $k^2 = \frac{n_r^2}{c^2}w^2$. For radiating solutions, the flow of energy by these waves through a point $\vec{r}$ at time t in the direction $\hat{n}$ is called the intensity (I), and is determined by the time-averaged Poynting vector $\vec{S}$, where:

$$\begin{aligned} \vec{S} &= \vec{E} \times \frac{1}{\mu}\vec{B} \\ I &= < \vec{S}\cdot\hat{n} >_\tau (\vec{r},t) = \frac{1}{2}\sqrt{\frac{\epsilon}{\mu}}|E_0|^2 \end{aligned} \tag{1.4}$$

While these are in principle vector equations, we will define a single axis of propagation $\hat{z}$ and assume a single polarization $\hat{\epsilon}_1 = \hat{x}$. this allows us to suppress the vector nature of the fields, the overall time dependent phase, and the magnetic component of the field . Moreover, since any real electromagnetic field can be written as a linear superposition of plane waves and each plane wave undergoes a linear transformation from one plane to another, we can write the electric (and magnetic) field at one plane as a linear transformation of some prior plane (Jackson, 1999):

$$\vec{E}_f(\vec{r}_f,t_f) = \iint \mathrm{G}(\vec{r}_f,\vec{r}_0,t_f,t_0)\vec{E}_f(\vec{r}_0,t_0)d\vec{r}_0 dt_0 \tag{1.5}$$

This general linear equation is the key to solving many (if not most) optical problems, for once the propagator G is determined, the field at any other point in space and time can be derived directly through equation 1.5. In an ideal imaging system the electomagnetic field is perfectly mapped point by point from one plane to another (up to magnification and overall multiplicative factors), so the propagator G is simply the Dirac delta function:

$$\vec{E}_f(\vec{r}_f, t_f) = \iint \delta(\frac{1}{M}\vec{r}_f - \vec{r}_0)\delta(t_f - (t_0 - \tau))\vec{E}_f(\vec{r}_0, t_0)d\vec{r}_0 dt_0 \tag{1.6}$$

Where the magnification $M = \frac{f_2}{f_1}$ accounts for rescaling the image and the time delay $\tau = \frac{c}{L}$ accounts for the time for light to transverse the microscope. In a standard 4f microscope imaging system, the temporal dynamics of the light are preserved to within a high degree of accuracy and we can ignore the overall temporal phase. However, spatial frequencies higher than the frequency of the light wave are non-radiative and suppressed entirely (as discussed in appendix A). The result is a system that does not fully reproduce the field in the focal plane: the resolution is limited to approximately $d_{res} = \frac{\lambda}{2NA}$, where the numerical aperature (NA) is given $NA = n_r \sin(\theta_c)$ by the highest input angle θ_c at which incident light can be accepted through the microscope (Mertz, 2010). As a result, a perfect δ-function reproduction of the object field is impossible. Instead, since the classical microscope has a linear propagator, we can characterize the imaging aberrations by their effect on a single point source located at the focal plane:

$$\vec{E}_f(\vec{\rho_f}) = \int CSF(\frac{1}{M}\vec{\rho}_f, \vec{\rho}_i)\vec{E}_f(\vec{\rho}_i)d^2\vec{\rho}_i \tag{1.7}$$

The goal of microscopy is to measure in some way the field $\vec{E}_I(\vec{\rho_I})$ and from that measurement determine the object field $\vec{E}_O(\vec{\rho_O})$. As such, ideally one would find a function CSF^{-1} such that for a measured field of some kind, we can perfectly reproduce the object:

$$\begin{aligned}\vec{E}_O(\vec{\rho_O}) &= \iint CSF^{-1}(\frac{1}{M}\vec{\rho}_O, \vec{\rho}_f)CSF(\frac{1}{M}\vec{\rho}_f, \vec{\rho}_i)\vec{E}_i(\vec{\rho}_i)d^2\vec{\rho}_f d^2\vec{\rho}_i \\ \delta(\frac{1}{M}\vec{r}_O - \vec{r}_i) &= \int CSF^{-1}(\frac{1}{M}\vec{\rho}_O, \vec{\rho}_f)CSF(\frac{1}{M}\vec{\rho}_f, \vec{\rho}_i)d^2\vec{\rho}_f\end{aligned} \tag{1.8}$$

Given a well-built microscope and an excellent understanding of its propagator, it would be possible to construct such an operator. However, real systems have aberrations, noise, and a lack of information. Such an operator cannot necessarily be constructed. Fortunately, a sufficiently good approximation can often be implemented. the question becomes how to best implement and approximate the ideal microscope, such that the object can be reconstructed. Since the equations governing the microscope transfer function are linear, we turn to the mathematics of linear inversion to extract the object information from the available measured information. As demonstrated throughout this thesis, increasingly minimal information requires increasingly sophisticated mathematics.

1.2 Modern Adaptive Optics

In order to optimize the information acquired by the microscope in a specific application, optimizing the mathematical reconstruction is best complemented by physical control of the light field hitting the detector. In particular, a Spatial Light Modulator (SLM) can be used to manipulate the amplitude or phase of the light in some plane, changing the CSF of the microcsope in a predetermined manner (Maurer et al., 2011; Booth, 2014). Using an SLM, we can manipulate the light to physically correct for aberrations (see Fig. 1·1), reducing the burden on computational and mathematical algorithms.

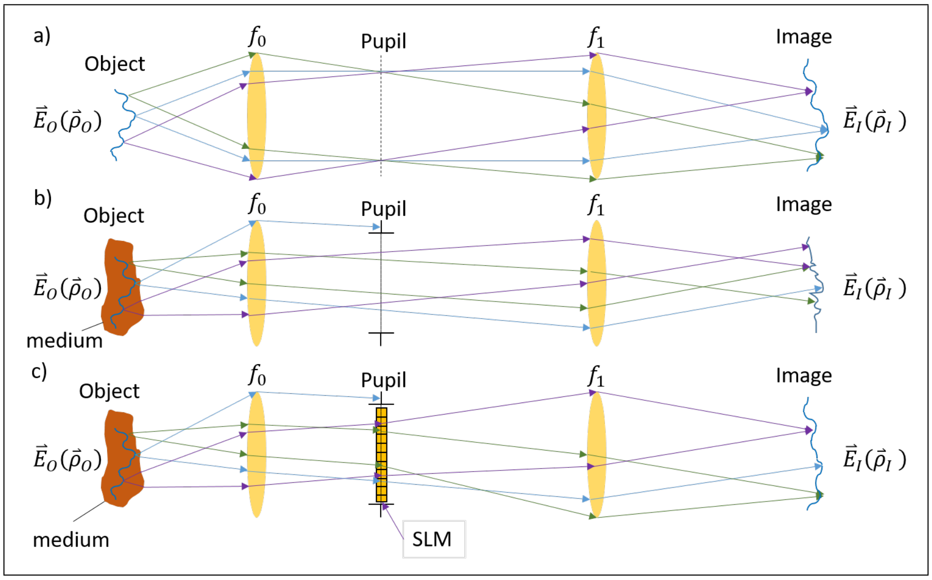
a)
Object
$\vec{E}_O(\vec{\rho}_O)$
f_0
Pupil
f_1
Image
$\vec{E}_I(\vec{\rho}_I)$
b)
Object
$\vec{E}_O(\vec{\rho}_O)$
medium
f_0
Pupil
f_1
Image
$\vec{E}_I(\vec{\rho}_I)$
c)
Object
$\vec{E}_O(\vec{\rho}_O)$
medium
f_0
Pupil
SLM
f_1
Image
$\vec{E}_I(\vec{\rho}_I)$

Figure 1·1: Implementing an SLM corrects for aberrations in an aberrated microscope

While transmissive SLM's abound, in all cases we use a reflective type of SLM called a Deformable Mirror (DM) for controlling the phase of the light. A DM is a reflective surface attached to posts that are controlled by electro-static actuators (Bifano, 2010; Stockbridge et al., 2012; Archer-Zhang et al., 2016). These actuators pull or push the reflective surface into different geometric positions; light reflecting off of the surface attains a local phase shift proportional to the mirror displacement (Fig. 1·2). The DM allows fast and achromatic control of the phase of light passing through the optical system at the modulation plane with minimal loss of transmission found in other SLM technologies (Yang et al., 2016). In particular, we place the DM in the pupil plane: while there are a number of configurations in which a DM is implemented for aberration correction (see for example (Li et al., 2015)), the pupil-plane configuration provides isoplanatic corrections to the system in that light from each point in the object passes through the pupil plane (Fig. 1·1). This simplifies the inversion of the linear process, as we wil see below (chapters 2-4)

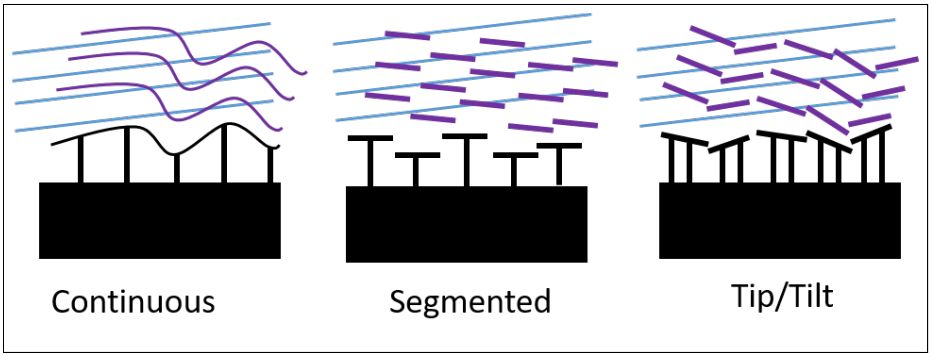

Figure 1·2: Deformable mirrors with different surface structures generate phase shifts in incoming light. Phase shifts are proportional to the local deflection of the DM surface, set by electrostatically controlled pistons.

This thesis is divided into 5 chapters (and associated appendecies). The first chapter (1) reviews the principles of optics required for modern optical microscopy, and the challanges faced in acquiring information about an object using an optical microscope. The second chapter (2) describes an adaptive-optics (AO) setup for imaging and ultimately tracking fluid flow in highly porous rock; scattering from the rock structure occludes the flow markers, and a Superpenetrative Multi-Photon Microscope (S-MPM) system is used to correct for the scattering in conjunction with a basic linear addition algorithm. The third chapter (3) describes a fast focal-scanning extended depth-of-field (EDOF) microscope for imaging volumetric dynamic samples; much of the sample is defocused, and the EDOF microscope is used to restore diffraction-limited resolution in conjunction with an open-loop deconvolution algorithm. The fourth chapter (4) describes a Matched-Filter Compressive Imaging (MFCI) flow cytometer for identifying cells and particles without chemical labels;

each cell population creates a unique scatter pattern, and the MFCI flow cytometer spatially separates and identifies the distinct scattering features in conjunction with a machine-learning (ML) algorithm. The fifth chapter reviews the balance between physically and computationally retreiving information from an aberrated optical system, and indicates potential directions for future exporations

Chapter 2

Basic Linearity in Optics

2.1 Fluid Flow in Porous Rock

Imaging inside a porous medium presents one of the most flagrant occlusions of information in optics. Light passing through a porous medium will scatter off the pore structure (Fig. 2·1), which typically is filled with a fluid of mismatched index and which varies in size and shape throughout the medium. The result is a completely randomized output wherein the emmitted fields exhibit Gaussian statistics, and the intensity has a Poissonian profile (Goodman, 2007). In a classical imaging system, any information about an object beyond or inside the medium is scrambled behind the randomization.

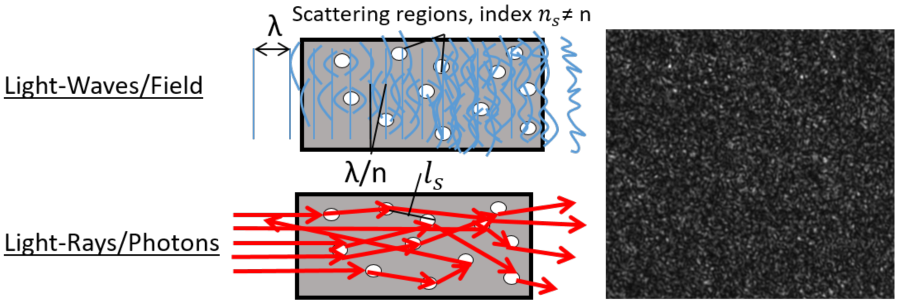

Figure 2·1: Schematic representation of light passing through a scattering medium, resulting in poissonian intensity fluctuations in the transmitted light (a form of speckle)

The inability to image in rock is a painful stumbling block for understanding the flow dynamics found in enhanced oil recovery. Enhanced oil recovery processes, such as fracking, have become a valuable tool for increasing oil production (Thomas, S., 2008). Water is pumped into the boundaries of the oil field, pushing out oil remaining in the microporous structure of the sedimentary rock. Understanding the flow properties of the oil-water mixtures is critical for optimizing production (Fredrich et al., 2006; Datta et al., 2013). Such an understanding can be obtained by visualizing the flow field using small fluorescent markers. However, tracking and analysing these markers is inherently challanging as they are embedded inside the porous medium, where the variations in refractive index between the rock and the oil/water fluid causes strong scattering (see appendix B for a discussion of the scattering properties of rock). The strong scattering of the rock medium has therefore limited the detailed study of the rock structures to the surface region only: attempting to image deeper into the rock structure requires removal of the surface layer (SHAH et al., 2017). This is impractical for studies of fluid dynamics critical to optimizing oil recovery.

Since the effects of aberrations depend on the characteristic length scales of the index variations, one natural solution is to image at longer wavelengths, where scattering is intrinsically weaker. While longer wavelengths provide inherently less resolution (see appendix A), this can be circumvented by taking advantages of non-linear effects in the imaging process. Multi-photon microscopy, and two-photon microscopy in particular, have proven invaluable in imaging deep within aberrating and scattering media, as the long-wavelength excitation combined with non-linear excitation allow for deep penetration into the medium with sufficient resolution (Crosignani et al., 2012; Ji, 2014). The low light-efficiency of the multi-photon process is circumvented by implementing a focus-scanning microscope: an incoming plane wave is focused down to a single point, which generates fluorescence at a higher wavelength than the excitation (Mertz, 2010). Such fluorescence is easily redirected and collected by using a dichroic filter and suitable detector. by scanning the point throughout the region of interest, we construct an image of fluorescence markers in the field of view.

2.2 Super-penetrative Multi-Photon Microscopy

Yet even though longer-wavelength systems can extend the viable imaging depth from the scattering length l_s to the transport-mean-free-path l^*, aberrations in many applications can still degrade image quality to the point of failure when imaging deep into the material. It then becomes necessary to remove the aberrations entirely, through either computational or physical means. Since multi-photon techniques are often light-limited, as the non-linear excitation process is rare, it is best to physically remove aberrations and restore optical power to the focal spot as much as possible. For non-linear processes, this can be done through a super-penetrative multi-photon microscopy (S-MPM) system (Tang et al., 2012; Paudel, 2015; Shain et al., 2015). In S-MPM, the scattering matrix acts as a position-dependent phase and amplitude mask at a single point in the sample. The field can be described through applying a linear transform acting on a uniform input field (Yu et al., 2013):

$$\vec{E}_f = \sum_i T_{fi} \vec{E}_i \tag{2.1}$$

For an isoplanatic region, the transfer function can be expressed as a pupil function acting on the Fourier representation of the fields (Mertz, 2010):

$$\vec{\mathcal{E}}_f(\vec{k}_\perp) = CTF_{rock}(\vec{k}_\perp) \cdot \vec{\mathcal{E}}_i(\vec{k}_\perp) \tag{2.2}$$

Where $\vec{\mathcal{E}}$ is the Fourier transform of the electric field ($\vec{E}$) and the coherent transfer function (CTF) is the fourier transform of the CSF in equation 1.7. To recover an unaberrated image, it is necessary only to correct the aberrated CTF applied to the light field by applying a physical transformation of the light that effects a linear multiplicative inverse:

$$\vec{\mathcal{E}}_i(\vec{k}_\perp) = \frac{1}{CTF_{rock}(\vec{k}_\perp)} \vec{\mathcal{E}}_f(\vec{k}_\perp) \tag{2.3}$$

We implement the direct light manipulation of equation 2.3 through a 1024 actuator segmented DM from Boston MicroMachines (BMC). The DM is placed in the microscope pupil plane (Shain et al., 2015), and a closed-loop optimization algorithm (Paudel, 2015) is applied to a deformable mirror that maximizes the intensity at a single point (Vellekoop and Mosk, 2007). Since aberrations shift power away from the focal point to the surrounding areas, we maximize the intensity at a single point by applying an orthogonal set of basis functions to the DM - in our case, Hadamard functions (Stockbridge et al., 2012). This can be done by applying a different phase to each pattern, and then using the linearity of the basis to reconstruct the optimal DM shape, redirecting light to the nominal focal spot (Fig. 2·2).

The result is improved imaging in a local field-of-view (FOV), as seen in figure 2·3. Unfortuantely, this improved imaging is only seen in a small corrected FOV. As we image through different parts of the rock, a new set of random features generates the scattering effects, and the correcting pattern applied to the DM is no longer correlated with the imaging point. The length of this correlation, defined by the optical memory effect (Berkovits and Feng, 1994; Judkewitz et al., 2015), determines the FOV attainable by a single correcting point.

In a fully scattering media such as porous rock, the width of the memory effect diminishes with thickness as $\frac{\lambda}{L}$, where L is the thickness of the rock. As seen in

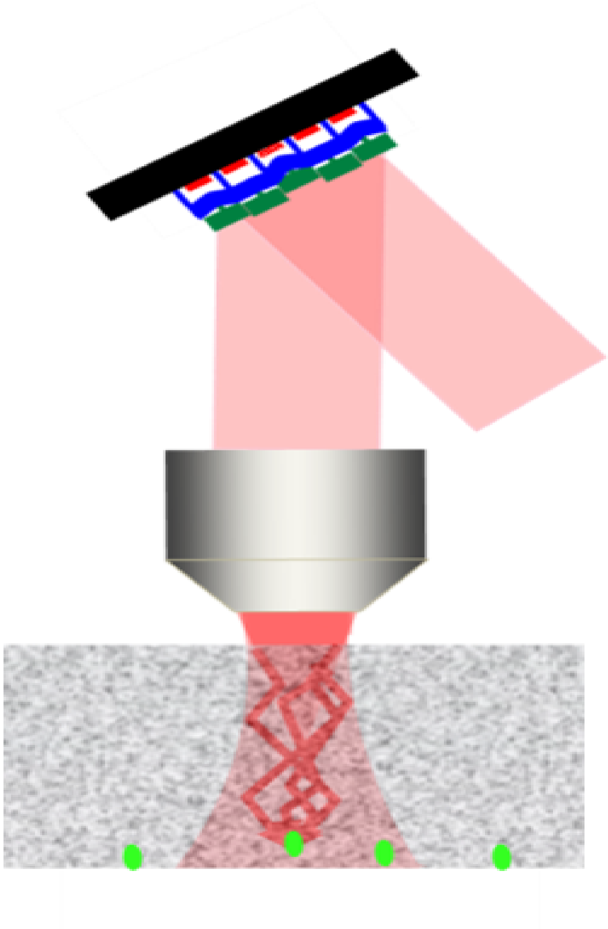

Figure 2·2: Deformable Mirror (DM) used to refocus light through scattering media to a single point

figure 2·4,while one can always correct for the effects of scattering at an arbitrary distance in the medium, the usable FOV about the correction shrinks to a diffraction-limited spot. While some flow statistics may be performed with only a single point of high-quality imaging, such a small field-of-view (FOV) is far from ideal for actually imaging the fluid flow. Despite being able to recover information about the sample at a single point by physically inverting the scattering process at that spot in the rock, imaging a large volume in the rock requires an additional innovation.

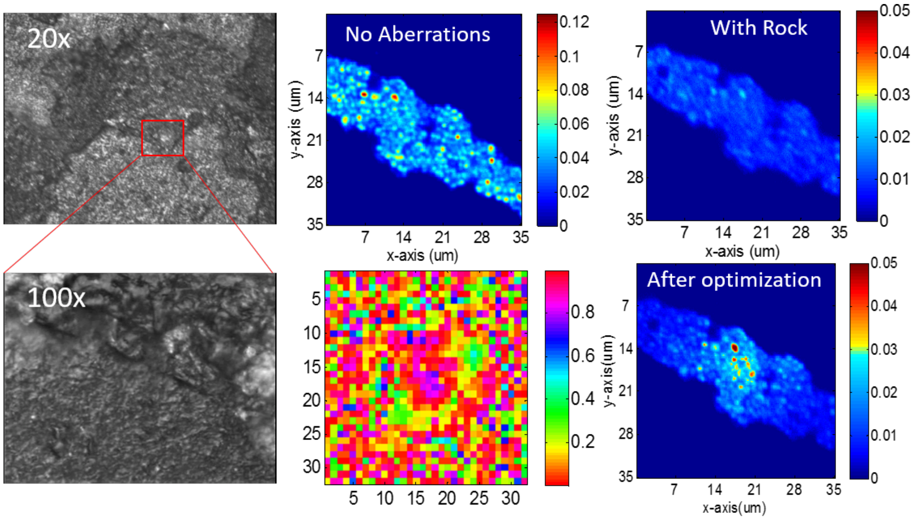

Figure 2·3: Aberration correction with an S-MPM Microscope

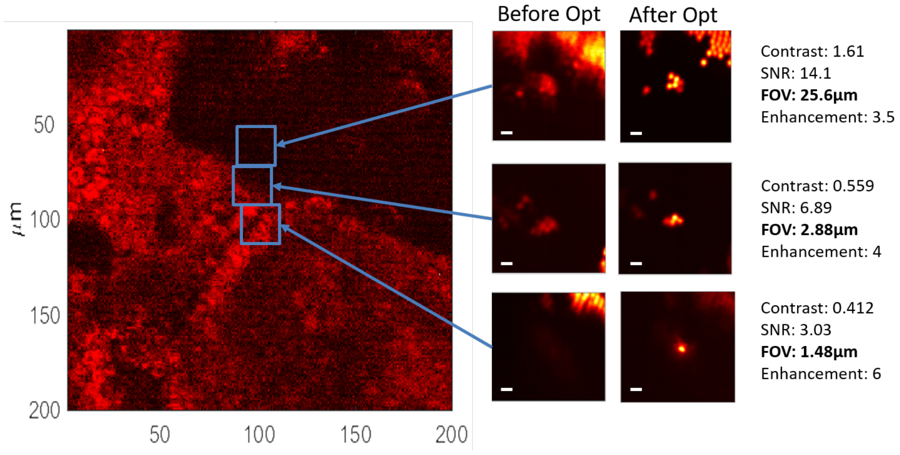

Figure 2·4: Left: 200μm x 200μm 2-Photon image of natural rock fluorescence from Arab-D rock surface , with 1μm fluorescent bead layer 100μm below (not visible). Right: Fluorescent beads before and after applying S-MPM correction.

2.3 Multi-Point Optimization

As mentioned in section 2.2, a usable FOV on the order of the diffraction limit is impractical at best. In order to obtain an improved image across the entire sample, one would need to determine the inverse phase map for each memory-effect correlated region, and then apply the correction dynamically while scanning over the volume of interest; in effect, breaking the CSF into local optimized components:

$$CSF_{net} = \sum_i \theta_i CSF_i \tag{2.4}$$

where $\theta_i = 1$ within the i^{th} optimization region and zero elsewhere. For biological samples this would be prohibitively time-consuming as the time needed to determine the full inverse map would be longer than the stability time of a given pattern. However, since the rock structure is static in time, we can develop a full imaging map for the entire region of interest (ROI), and successfully apply it to image inside the rock using a high-speed deformable mirror. The result is a patchwork image of isoplanatic patches (Fig. 2·5) built out of the optimal CSF in each region.

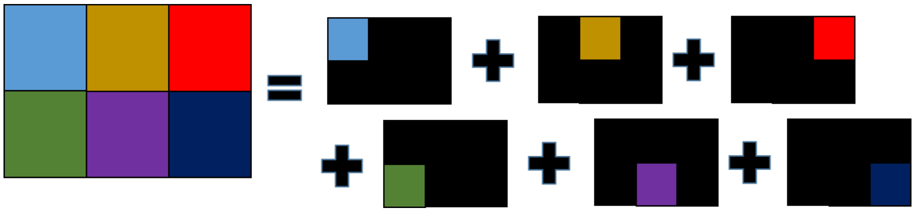

Figure 2·5: Diagramical representation of MPO solution

We therefore developed a technique to increase the field-of-view when using our current S-MPM setup to expand our FOV when imaging in rock. If we begin with a FOV larger than the spacing between beads (or any source for optimization), we can jump from one bead to another and generate a Multi-Point Optimization (MPO) map. Since the scattering properties of the rock remain constant even under dynamic flow conditions, we can update the DM to the appropriate pattern for a given pixel without re-optimizing each image. In this way we can pre-optimize a large volume of the rock, which would enable us to track nanoparticles through an arbitrarily large portion of the rock sample at a frame rate limited only by our scanning speed.

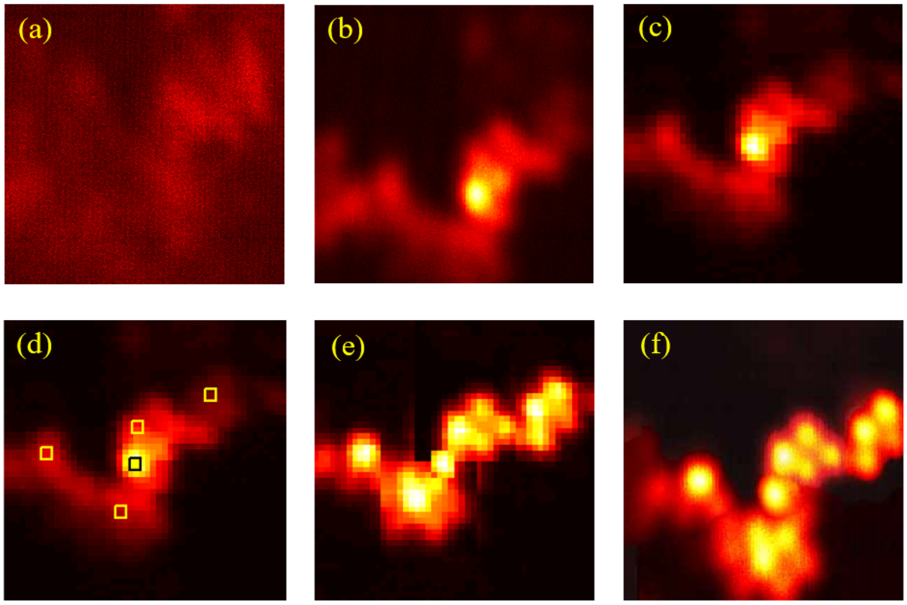

Figure 2·6: Stitch imaging of 1μm beads. Field-of-view is 10μm x 10μm. (a) without correction, (b) single optimized sweep image (c) step scan is shown, (d) local maxima, (e-f) manual stitching of five images.

We imaged 1μm fluorescent beads directly under the 67μm thick Saudi Aramco rock filled with mounting wax. Figure 6(a) shows beads without correction, Figure 6(b) shows an optimized image when beam was parked at the center of the image, with an approximately 1μm FOV. In order to map exact galvo position of each image pixels, we rescan with 50x50 pixels step scan (the step scan image is shown in Figure 6(c)). The slight shift in the image center was due a systematic offset between zero positions at the two scanning modes (parked beam and sweep beam). A list of local maxima was calculated from the initial scan image which are plotted in Figure 6(d). Using these exact galvo positions we found optimized voltage maps of deformable mirror (DM) for each local maxima. Figure 6(e) and Figure 6(f) are the images produced by manually stitching of five optimized images from step scan and sweep scan respectively, demonstrating a 10m FOV.

In practice, it would be possible to change the DM pattern while scanning, providing a full field-of-view with no loss of framerate. The DM pattern would be determined by the galvo scan position and the appropriate inverse solution given above. We see that by using a physical correction at a large number of points in the rock to restore the acquired sample information, the technique needed to piece together the full image structure is a simple linear equation. Moreover, a high-speed SLM is critical for actually implementing the correction; if the SLM is significanly slower than the scanning mirrors, then the whole system becomes limited by the operating speed. In fact, for a fast enough SLM, one could imagine implementing an open-loop measurment of the coherent scattering function via a wavefront sensor and implementing MPO at biological timescales.

Chapter 3

Deconvolution Algorithms and Applications

3.1 Dynamic Volumetric Imaging

Many samples of interest have dynamics that occur over large volumes and short timescales. These dynamic volumetric samples, such as neuronal activity in brains (Gong et al., 2015; Ji et al., 2016; Yang and Yuste, 2017), bacteria in their natural environment (Frentz et al., 2010; Bishara et al., 2011; Wang et al., 1960; Zhuang and Sitti, 2016; Constantino et al., 2016), tracer molecules describing fluid flow (Memmolo et al., 2015; Chen et al., 2017), and even flame plumes (Carter et al., 2016), all require images of the full volume at high resoluion and high speed to fully describe the sample. An imaging system capturing such an extended dynamic sample must therefore record a large volume at high resolution and high speed in order to obtain features of interest.

An ideal 3D imaging system would map each point in the volumetric object to a unique point in the system output:

$$I_j = \sum_i \delta_{ji} O_i \tag{3.1}$$

Modern cameras, unfortunately, are two-dimentional rather than three-dimensional: they can only measure information along a single plane. This in and of itself would not be a problem if cameras directly measured the electric field, which obeys a linear transfer equation that would (theoretically) allow full recovery of the volumetric region of interest. However, current cameras directly measure only the amplitude of the field stripped of the phase component. Moreover, the sources of interest are points that emit mutually incoherent light, so the fluctuations in the electromagnetic field needed to reconstruct the full volumetric ROI are quickly averaged out. For a standard microscope system there is a linear propagation of intensity from the object to the camera given by:

$$I(\vec{x}_I) = \int PSF(\vec{x}_I, \vec{x}_O)O(\vec{x}_O)d\vec{x}_O \tag{3.2}$$

Where the convolution kernel, called the point-spread function (PSF), represents the transfer function of a 2-D plane. In a classical imaging system, only the focal plane is fully reproduced as accurately as possibile: objects outside the focal plane are aberrated by defocus. This limits acquisition to a thin depth-of-field (DOF) where the objects are in-focus, preventing researchers from fully reproducing the volume dynamics. No such classical imaging technique is capable of full volumetric recovery at high speed and high resolution in a simple manner. There is therefore a strong need for an easily implementable imaging method that provides high-resolution and high-framerate volumetric images.

3.1.1 Extended Depth-of-Field with Axial Scanning Microscope

One solution is to create an extended depth-of-field (EDOF) microscope system that maintains lateral resolution over a long axial range (Welford, 1960; Hausler, 1972; Indebetouw and Bai, 1984). An EDOF can be implemented in either scanning (Dufour et al., 2006; Lu et al., 2017) or widefield (Abrahamsson et al., 2006; Dowski and Cathey, 1995; Grewe et al., 2011) systems, creating an axially-invariant extended PSF (EPSF) by manipulating how the light passes through the system. We implement the extended depth-of-field by placing a DM in the focal plane of the microscope and applying a parabolic shape to the DM surface (Fig. 3·1). This shifts the focal plane of the microscope by a distance $Z = -nf_2^2/(M^2 f_{DM})$ in the sample, where f_{DM} is the focal length associated with the DM shape and n is the index of refraction in the sample (Giese et al., 2014). The DM can change curvature at over 20kHz, allowing us to bring over 20 planes of the sample into focus on the camera in the timespan of a single kHz-rate camera frame. Applying a stroke S to the DM results in a shift in the focal plane of a distance:

$$Z = 4n\left(\frac{f_2}{MR_{DM}}\right)^2 S \tag{3.3}$$

Sweeping over a large stroke range ΔS results in an image of the sample intensity compressed by integrating over the axial direction (Shain et al., 2017b). For well-separated point like objects, this technique is sufficient to fully recover the lateral locations of the objects in the volume of interest and they can be easily localized under the EDOF microscope (Fig. 3·2a,b). This can be attributed to the lateral shape of the EPSF: it has approximately the same gaussian shape near the lateral intensity peak and the same full-width at half maximum (FWHM) as a classical PSF (Fig. 3·2d). For sparse structures where only the centroid information is needed to recover the object, simply physically extending the PSF in the axial direction is therefore sufficient.

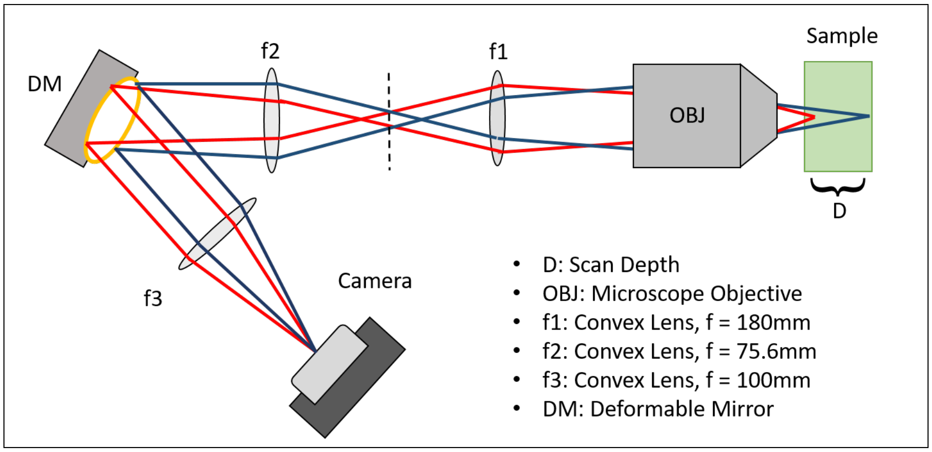
DM
f2
f1
Sample
OBJ
D
f3
Camera
D: Scan Depth
OBJ: Microscope Objective
f1: Convex Lens, f = 180mm
f2: Convex Lens, f = 75.6mm
f3: Convex Lens, f = 100mm
DM: Deformable Mirror

Figure 3·1: Schematic of EDOF Microscope. Vertical dashed line indicates location of intermediate image plane.

3.2 Open-Loop Deconvolution

When imaging denser structures, centroiding is insufficient: the object is described by the precise intensity at each point. However, the contribution from the long tail of the extended PSF occludes that information, resulting in a haze that blurres the object (Fig. 3·3). Fortunately, the contributions to the background haze are linear combinations of the sample itself convolved with the PSF, and the process can be inverted through deconvolution (Bertero and Boccacci, 1998). Since the imaged intensity is a convolution of the PSF with the object, taking a Fourier transform of the image and applying the Fourier convolution theorem (Katz et al., 2014; Lu and Hua, 2015) reduces equation 3.2 to a simple linear multiplication problem:

$$\begin{gathered} F[I](\vec{k}_\perp) = OTF_{\vec{k}_\perp} \cdot F[O](\vec{k}_\perp) \\ O = F^{-1}\left[\frac{F[I]}{OTF}\right] \end{gathered} \tag{3.4}$$

Where the optical transfer function (OTF) is the Fourier transform of the PSF: $OTF = F[PSF]$. This is the same linear transfer equation as equation 2.3, and

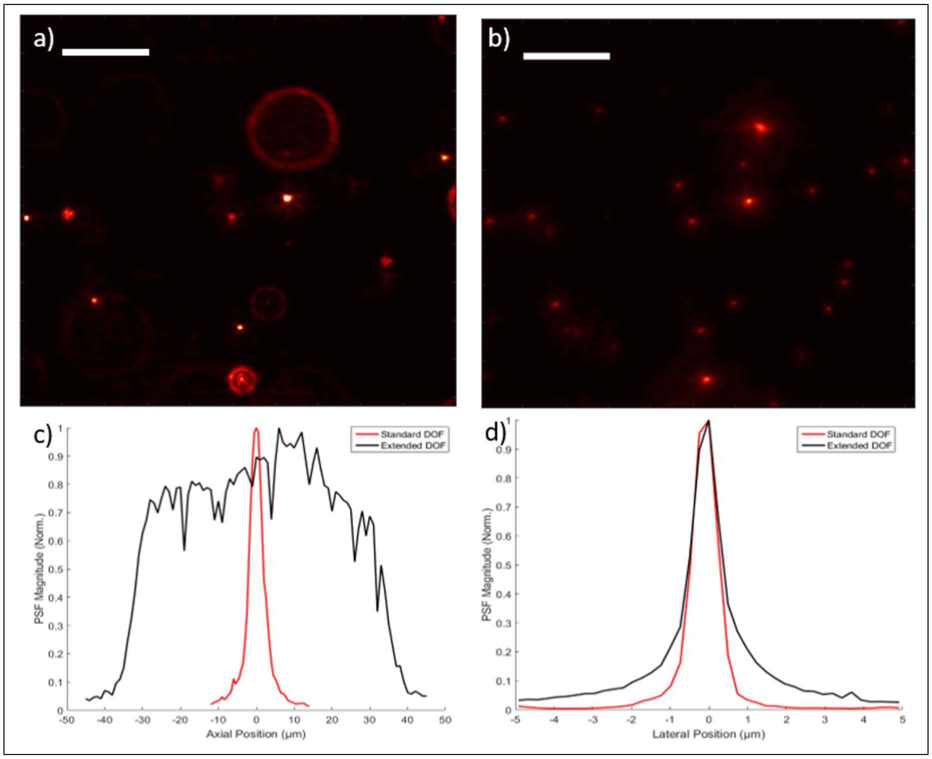

Figure 3·2: Classic vs. EDOF microscope imaging of 1μm diameter fluorescent beads embedded in PDMS. Images taken with 20× 0.5NA objective; EDOF=70μm with 26 DM frames. Beads that are defocused in the standard image (a) reappear in the EDOF image (b). Normalized axial PSFs for classic and EDOF microscope demonstrate significand increase of the DOF under focal scanning (c). Lateral PSFs for classic and EDOF microscope are shown in (d), illustrating that while EDOF maintains the lateral resolution as defined by the FWHM it increases the surrounding intensity as well. Scale bar is 25m.

ideally would be solved similarly; indeed, so long as the OTF is well defined, the object can be recovered by simple division by the OTF on both sides. When the OTF approaches zero, however, division by the OTF over-amplifies the corresponding spatial frequency of the object. This introduces noise at that spatial frequency to the reconstructed object. In such a case, the raw OTF cannot be used as-is: it must be regularized to ensure physically viable outputs from a given input. We use Weiner deconvolution with Tikonov regularization (Bertero and Boccacci, 1998), wherein an additional term δ is added to the denominator in such a way as to reduce the amplification of noise:

$$O_{est}(\vec{x}_O) = F^{-1}\left[\frac{OTF^*_{\vec{k}_\perp} \cdot F[I](\vec{k}_\perp)}{|OTF|^2 + \delta^2}\right] \tag{3.5}$$

For large values of the OTF, equation 3.5 reduces to equation 3.4. The advantage of this regularization is that in the event that the OTF goes to zero, the denominator reduces to a non-zero value. This is always the case at high spatial frequencies due to the diffraction limit, and is potentially the case at any other spatial frequencies depending on the system-specific OTF. In theory the parameter δ is chosen to be the spectral density of the noise (Lu and Hua, 2015; Meitav et al., 2016), so that noise at a given frequency is not overamplied, but in practice δ is often taken as a constant that is chosen by visual adjustment of the deconvolved images (Shain et al., 2017b).

3.2.1 Deconvolving Extended Depth-of-Field Images

In order to implement deconvolution some assesment of the OTF must be made, either through measuring or calculating the PSF (open-loop deconvolution), or through estimating the OTF by indirect constraints (blind deconvolution). For the EDOF

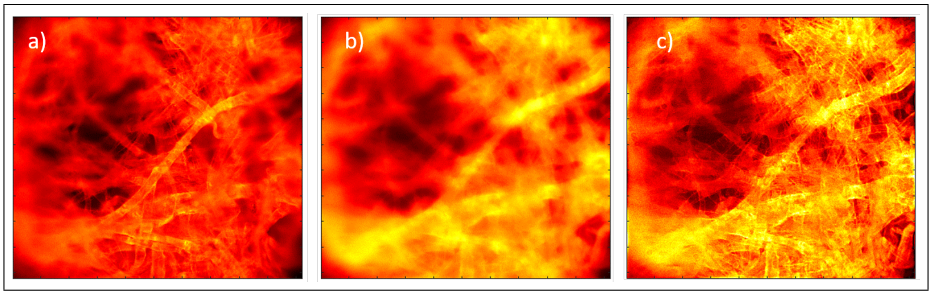

Figure 3·3: (a) A classical microscope image of tissue marked with fluorescent highlighter shows intricate detail in a small in-focus region and a blurred object elsewhere. (b) An EDOF image uniformly blurs the object, occluding it throughout the FOV. (c) EDOF with deconvolution removes the blur across the image, restoring full resolution to the parts of the objcet within the scan range ($D = 70\mu m$); parts of the object outside the scan range remain blurred, as the EDOF model for the OTF does not take them into account.

microscope, we derived a formal approximation for the extended OTF (EOTF) of any object within the scan range (Shain et al., 2017b):

$$EOTF(k_\perp; D) \approx \min \begin{cases} \frac{2}{\pi}\Big(\cos^{-1}\frac{k_\perp}{\Delta k_\perp} - \frac{k_\perp}{\Delta k_\perp}\sqrt{1-|\frac{k_\perp}{\Delta k_\perp}|^2}\Big) \\ \frac{4k}{\pi D \Delta k_\perp^2 \frac{k_\perp}{\Delta k_\perp}}\sqrt{1-|\frac{k_\perp}{\Delta k_\perp}|^2}, \end{cases} \tag{3.6}$$

Where $\Delta k_\perp = 2NA/\lambda$ is the bandwidth of the microscope (Mertz, 2010). From equation 3.6, the EOTF of the optical system acts as a low-pass filter: higher spatial frequencies are blurred into lower ones by combining in-focus and defocused realizations of the object. Inserting the EOTF of equation 3.6 into equation 3.5 implements a properly tuned high-pass filter, and by choosing an approprate value for δ ($0.01 < \delta < 0.1$), we can obtain an improved image of the dense structure (Fig. 3·3). Note that not all of the image has been deconvolved successfully: parts of the object that lay outside the scan range remain blurry (Fig. 3·3c), as the EOTF does not accurately describe the intensity transfer function for those parts of the sample.

A final consideration is that the EOTF, while extending over a large axial range, is still a 2D transfer function. It can be used to improve the lateral resolution, but cannot recover any depth information about the object. Indeed, all the information about the object's depth is removed from the system by the axial scanning process, which compresses the three-dimensional object into a two-dimensional image. This dimensionality reduction makes the linear system inherently non-invertible. As a result, more sophisticated techniques are needed to recover the three-dimensional information of the object.

3.3 Axial Localization with Modulated Illumination

One method to recover axial information from an EDOF-style microscope is to modify the physical microscope system by forcing the PSF to depend on the axial position. While there are a number of different techniques that can be used to create such an axially-varying PSF (Llull et al., 2015; Berlich et al., 2016), a particularly easy implementation is to simply vary the illumination power during the focal sweep. The illumination source (usually a laser or LED) can typically be modulated faster than any other component in the system, and control can be achieved with a function generator synchronized to the DM modulation rate without further modification to the EDOF microscope setup shown in fig. 3·1. The most basic modulation is a linear ramp, and by acquiring two frames in succession - one modulated to linearly increase the intensity over the focal sweep (I_m), and one with the modulation static (I_0) - we can recover both the deconvolved axially-averaged intensity $O(\vec{x}_0)$ and the intensity-averaged axial position $h_{z_0}(\vec{x}_0)$ of the object at each point (see appendix D for full derivation):

$$\begin{aligned} O(\vec{x}_0) = \int O(\vec{x}_0, z_0)\mathrm{d}z_0 \qquad &= F^{-1}\left[\frac{\tilde{I}_0(\vec{k}_\perp, D)}{L_0 EOTF(\vec{k}_\perp, D)}\right] \\ h_{z_0}(\vec{x}_0) = \frac{\int z_0 O(\vec{x}_0, z_0)\mathrm{d}z_0}{\int O(\vec{x}_0, z_0)\mathrm{d}z_0} \quad &= \frac{F^{-1}\left[\frac{\left[\tilde{I}_m(\vec{k}_\perp, D) - \tilde{I}_0(\vec{k}_\perp, D)\right]}{m\left[MOTF(\vec{k}_\perp, D)\right]}\right]}{F^{-1}\left[\frac{\tilde{I}_0(\vec{k}_\perp, D)}{L_0 EOTF(\vec{k}_\perp, D)}\right]} \end{aligned} \tag{3.7}$$

This axial localization with modulated illumination (ALMI) technique calls for a slight improvement in our regularization parameter. With a static illumination the EOTF goes to zero only at high frequency, and so the regularization parameter can be set based on the high-frequency noise alone, allowing us to use a constant value for δ. However, the modulated OTF (MOTF) appering in equation 3.7 goes to zero at both high and low spatial frequency, necessitating a regularization parameter that varies between those limits (see Fig. 3·4). These zeros are fundamental to the microscope system: just as the decay of the EOTF at high spatial frequency arises from the effects of diffraction (see section 3.2.1), the zero value of the MOTF at low spatial frequency is connected to the lack of sectioning (Mertz, 2010) in linear microscope systems. Instead of using a constant value for δ, we implement a step function with different low-frequency and high-frequency values:

$$\delta(\vec{k}_\perp) = \begin{cases} \delta_1 & (k_\perp > k_c) \\ \delta_0 & (k_\perp < k_c) \end{cases} \tag{3.8}$$

where k_c is a cutoff frequency separating the high and low frequency regimes (typically chosen where EOTF and MOTF intersect). In general, we found that δ_0 could be chosen much smaller than δ_1. This could be related to the low-frequency region (where MOTF is small) covering much less $k_\perp$-space area than the high-frequency region (where both MOTF and EOTF are small); this could be causing the presence of noise in the low-frequency region to be less detrimental. In all cases, the specific values of δ_0 and δ_1 were chosen by eye.

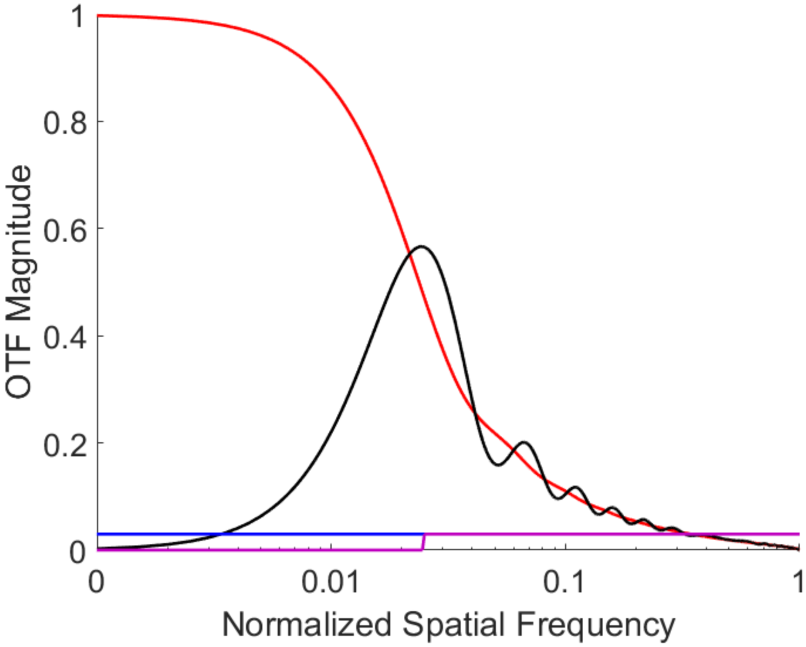

Figure 3·4: EOTF (red) and MOTF (black) curves for a focal scan range of 60μm, as a function of spatial frequency normalized to the diffraction limit. Example regularization parameters (blue, purple) are shown for reference.

3.3.1 Experimental Validation

We experimentally evaluate the accuracy of our axial localization with modulated-illumination (ALMI) strategy by measuring the effect of the deconvolution corrections used in equations 3.7. For this comparison, we introduce the naive depth estimator:

$$h_u\left(\vec{x}_0\right) = \frac{D}{2} \frac{I_m\left(\vec{x}_0\right) - I_0\left(\vec{x}_0\right)}{I_0\left(\vec{x}_0\right)} \tag{3.9}$$

To verify the accuracy of the axial co-ordinate, we measured the position of 1μm diameter fluorescent beads while axially translating the beads with a separate mechanical stage. A Thorlabs M470 L3-C Blue LED was used to generate fluorescence at about 500nm, and an Olympus BX51 microscope with a 20x, 0.5NA objective was used to collect the light, giving a classical depth-of-field of about 2μm. We used a 140-actuator Multi-DM from Boston Micromachines Corporation (BMC) to generate a total scan range of D=60μm.

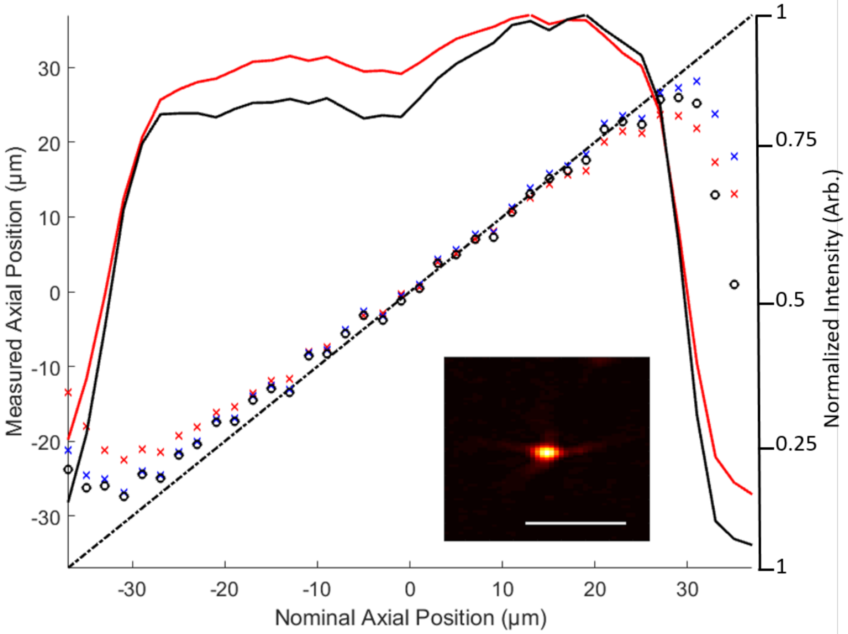

Figure 3·5: Verification of axial localization with an isolated 1μm bead (inset). Scale-bar is 5μm. Intensity of the bead as a function of stage position before (solid red) and after (solid black) deconvolution illustrates the range of the extended DOF of about 60μm. Axial localization of the bead before deconvolution (red) shows good agreement with the nominal stage position (dotted black) over the extended DOF (slope $\approx$ 0.8, $r^2 = 0.996$). Axial localization with a single (blue) and double (black) parameter deconvolution shows improved axial accuracy (slope $\approx$ 0.9, $r^2 = 0.997$).

For isolated beads (Fig. 3·5), both $h_u(\vec{x}_0)$ (Eq. 3.9) and h_{z_0} (Eq. 3.7) provide accurate axial localization over the focal-scan range. Outside this range, the accuracy of the axial localization decreases dramatically, as the ALMI model no longer applies. However, for larger lateral structures such as groups or rafts of beads (Fig. 3·6), axial localization values can only be accurately recovered when applying the deconvolution algorithm of equation 3.7. In other words, while deconvolution is not required for sparse, point-like objects, it becomes critical for laterally extended objects. In fact, because the noise level at low spatial frequencies is better than at high spatial frequencies, laterally extended objects can be accurately estimated even beyond the scan range.

While we used fluorescent sources to verify the ALMI technique, any incoherent imaging modality with the above OTF can be easily adapted for volumetric imaging. To demonstrate the sufficiency of arbitrary incoherent illumination (with an axially symmetric response) for this technique, we imaged 4μm fluorescent beads suspended in PDMS with both fluorescent and dark-field illumination modes. A Thorlabs M625 L3 Red LED was used to provide additional darkfield illumination from below the 4μm bead sample, allowing for easy comparison between the two imaging modes (Fig. 3·7a,b). Fluorescence and darkfield images give identical relative positions for each of the 4μm bead samples, with an offset between the two imaging modalities of about 3.2μm (Fig. 3·7c). This offset is slightly larger than the nominal resolution given by the classical depth-of-field, however this is due to a slight shift observed in the nominal focal plane, likely caused by changing the imaging wavelength from 500nm to 625nm.

Figures 3·5, 3·6, and 3·7 illustrate the capacity of our ALMI technique to perform axial localization of both fluorescent and non-fluorescent objects. A crucial requirement for this localization, however, is that the objects do not overlap one another in the axial direction. In the event such overlap occurs, our technique returns an overall intensity-weighted average of the depth (per equation 3.7). For example, if two point-like objects lie at the same lateral position but at different depths z_1 and

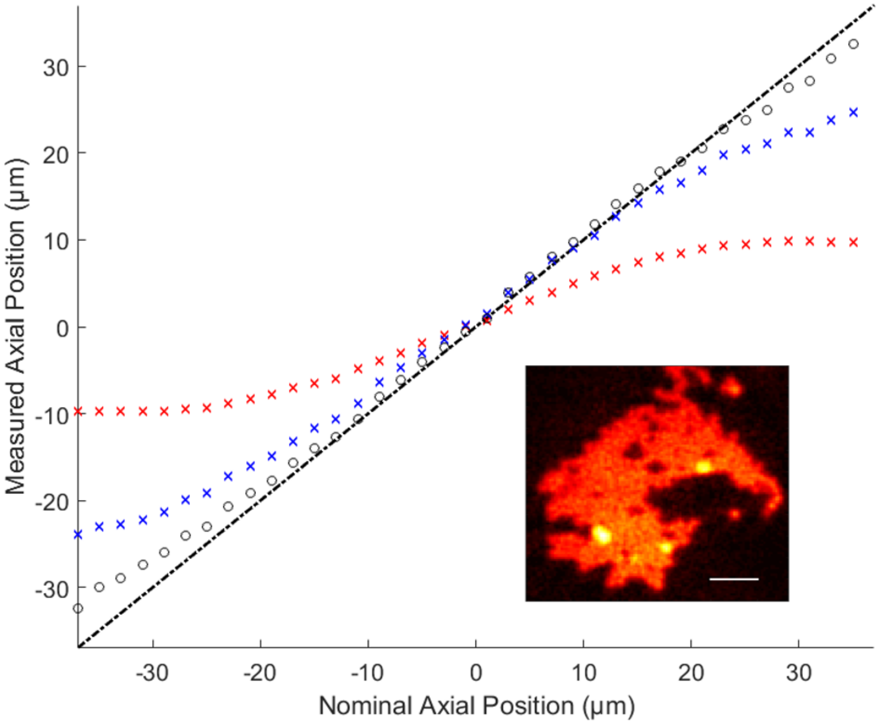

Figure 3·6: Verification of axial localization with an extended cluster of 1μm beads (inset). Scale-bar is 5μm. Axial localization of the cluster before (red) deconvolution shows linearity but poor accuracy in estimating the axial position within the DOF, systematically underestimating deviations from $Z = 0$ (slope ≈ 0.4, $r^2 = 0.983$). After applying deconvolution (blue) with a single regularization parameter the accuracy improves significantly (slope ≈ 0.8, $r^2 = 0.998$). Two-parameter deconvolution (black) provides even higher accuracy (slope ≈ 0.9, $r^2 = 0.999$) which extends even beyond the focal scan range of 60μm.

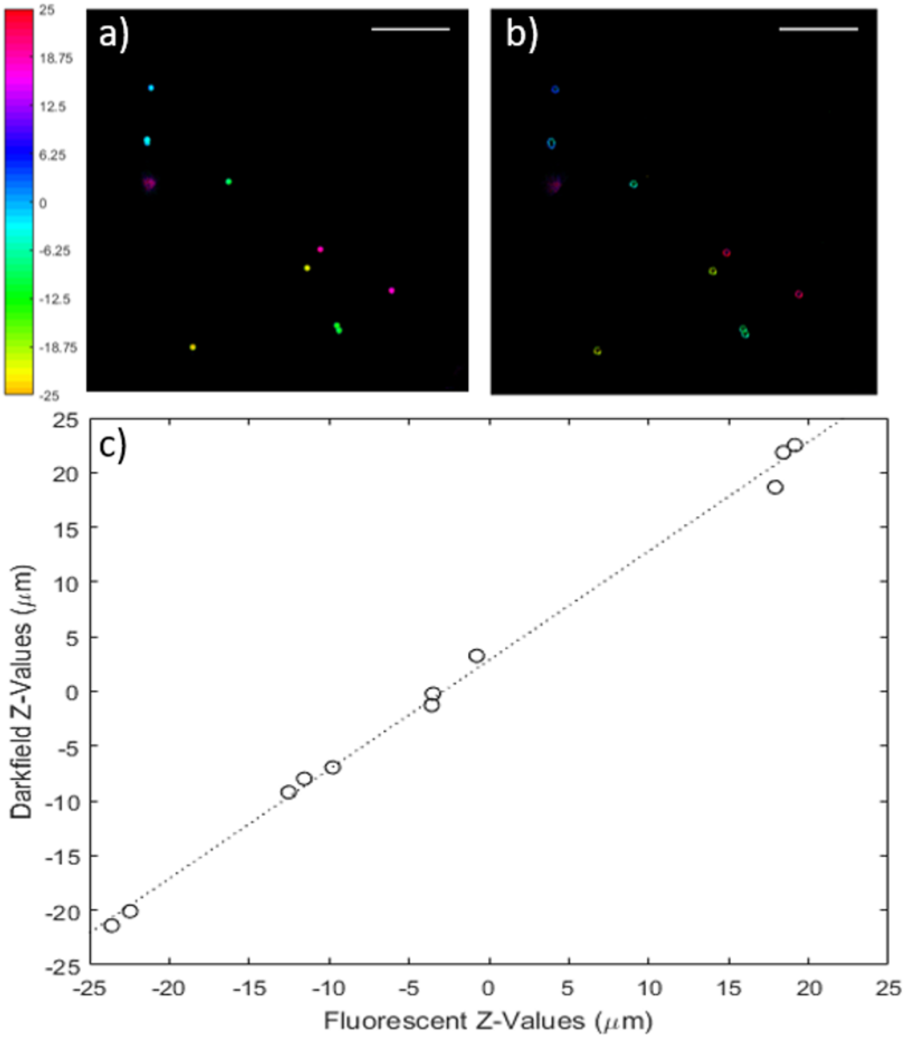

Figure 3·7: MI-EDOF images of 4μm beads embedded in PDMS acquired with fluorescence (top left) and darkfield (top right) imaging modes. Axial displacement from nominal focus is represented by the color axis (in units of microns); scale bar is 50μm. Comparison of the axial positions obtained in fluorescence and darkfield modes is also shown (bottom), yielding a linear fit of slope 1.02, and offset 3.2μm.

z_2, our technique returns an image of only a single object located at an apparent depth $(z_1 + z_2)/2$. This weighted-intensity axial localization is apparent in Fig. 3·8, which shows a darkfield image of a cylindrospermum algae (Carolina Biological Supply) suspended in water. The algae is generally sparse enough to identify the depth profile of individual strands; where the strands overlap, the depth is identified as an intensity-weighted average axial position. Since we use a single-shot deconvolution method to obtain the heights, any overlapping parts of the object skew the recovered position, whether or not they are within the scan range. This also underscores the limitation of the open-loop deconvolution technique in general, in that where objects extend beyond valid regime for modelling the PSF, even the parts of the object within the scan range may not be fully recovered. To account for such extended objects, more advanced techniques are required (see section 3.4).

3.3.2 Discriminating Neurons with Depth Information

Fortunately, for many applications full quantitative 3D imaging is not required. Functional neuron imaging in particular requires only a semi-quantitative assessment of depth, as the depth parameter is used primarily to distinguish overlapping neurons that fire simultaneously. Since the neurons blink both independently and in-sync, it is possible to identify a given neuron or a combination of neurons is firing by looking at the relative apparent depth of the neuron in time. We demonstrate this in figure 3·9, which shows neuronal activity of two distinct overlapping neurons taken with an ALMI microscope system. Intensity plots of the overlapping (purple) and non-overlapping (green, blue) regions show that the overlap region exhibits calcium transients associated with either neuron (Fig. 3·9a-b). However, the overlap intensity alone would not be sufficient to enable the association of a particular transient to a particular neuron, without recourse to statistical correlations over non-overlapping

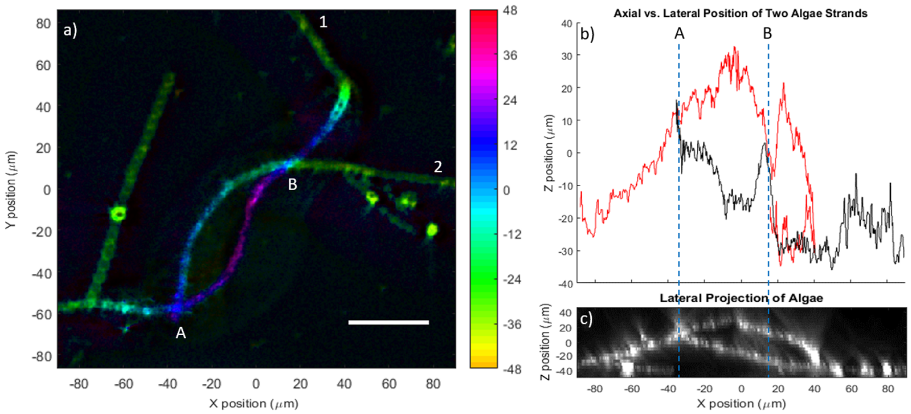

Figure 3·8: Cylindrospermum algae acquired with ALMI in dark-field mode using a 20× 0.5NA Olympus objective (left). From the modulated-illumination image, two algae strands appear to overlap at two distinct points (A and B). Plots of the recorded axial location of each strand (top right) near point B reveal sharp variations that converge to a common axial location, indicative of an incorrect apparent co-localization of the strands. The convergence at point A occurs at much more slowly, suggesting the two strands are in fact co-localized at that point. This is verified by an x-z projection obtained from an image stack, where we confirm that the strands are axially co-located point A but axially separated at point B. The different behaviors of axial plots about these points suggests that with prior information about the sample (such as continuity constraints), correct axial information can be inferred even in non-co-localized cases.

regions (Inglis et al., 2008; Theis et al., 2016). Using our axial localization technique, analysis of the axial positioning data (Fig. 3·9c) indicates that when the green neuron fires, the apparent depth of the overlap increases (Fig. 3·9d1), whereas when the blue neuron fires, the apparent depth decreases (Fig. 3·9d3). When both neurons are simultaneously active, the depth appears unchanged (Fig. 3·9d2), since our technique provides the intensity-averaged axial position as indicated in Fig. 3·8. In other words, the association of calcium transients to specific neurons can be achieved locally using information obtained from a single image point, rather than requiring delocalized cross-correlations obtained from spatially separated image points.

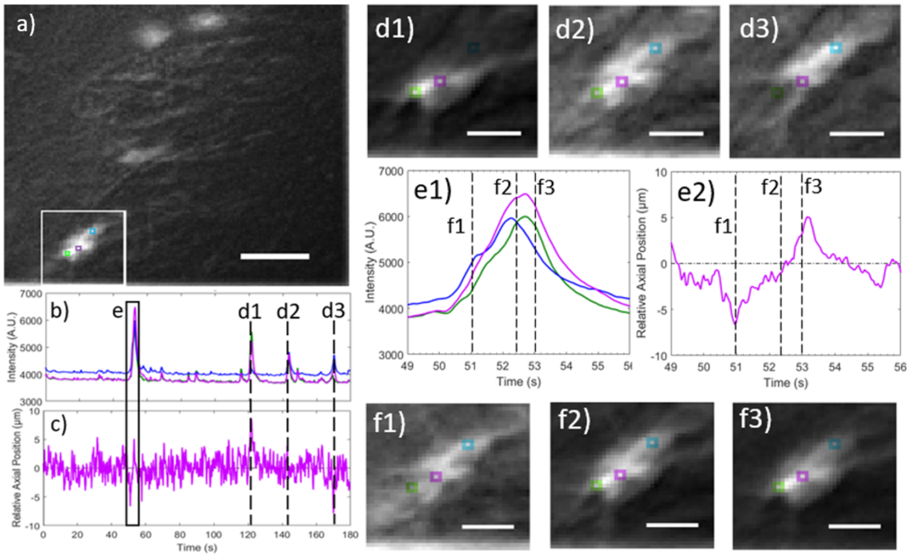

Figure 3·9: a) In-vivo ALMI data from GCaMP-labeled neurons in a mouse striatum (three frames are shown from a video). Distinct neurons are observed (blue, green) in the indicated ROI that laterally overlap (purple); scalebar is 50μm. b,c) Intensity and depth variations are monitored simultaneously, facilitating the discrimination of neuronal activity. d1-3) ALMI video frames show neurons firing either individually or together; scalebars are 20μm. e1-2) Intensity and depth of neurons firing almost simultaneously. f1-3) ALMI video frames show near-simultaneous firing of neurons; scalebars are 20μm

3.4 Blind Deconvolution

The ALMI technique, and EDOF techniques in general, rely on the assumption that the sample is enclosed entirely within the scan range. For sparse objects, even those extended over a large volume, this is a reasonable approximation in that parts of the sample outside the scan range are dim and ultimately negligible. For densly packed objects, this assuption breaks down and sources outside the scan range begin to contribute meaningfully to the EDOF image. An important example is with fluorescent brain imaging, in which there are two secondary effects that contribute to the image arising from objects beyond the scan range: defocused fluorescent and defocused absorbing structures (Shain et al., 2017c). Defocused fluorescent structures deep within the brain combine to contribute a (mostly) uniform fluorescent haze, acting like a trans-illumination source that reduces the SNR; this back-illumination cannot be deconvolved through the open-loop methods above (section 3.2). If the static background were the only effect of the deep fluorescence, it could be treated as an overall offset and subtracted before deconvolving the image. Yet because of the trans-illumination coming through the sample, defocused absorbing structures within the brain (such as blood vessels) become visible. Absorbing structures within the scan region can be treated as objects of negative fluorescence; however, objects located close enough to the scan region to be distinguished but too far outside the region to be modelled accurately by the EOTF cannot be accounted for in the EOTF approximation. Since open-loop deconvolution treats the image as if it has a uniform PSF, the 2D acquisition of the images precludes the ability to distinguish parts of the object within the scan range from parts of the object outside that range. It is fundamentally unable to account for these additional structures.

3.4.1 Dual fluorescence-absorption deconvolution

Since open-loop deconvolution is insufficient, a more advanced mathematical formulation is necessary. Rather than obtaining the object structure in a single-shot from a closed-form expression containing our knowledge of the OTF, we use a metric ϵ that models the OTF to iteratively optimize our estimate of the object, where ϵ is given by:

$$\epsilon = ||I - O * PSF||^2 \tag{3.10}$$

Where in theory both the PSF and the object O can be estimated in a given model (Bertero and Boccacci, 1998). Open-loop deconvolution can be seen as a special case of this framework, where the PSF is precicesly modeled for the entire object and so the optimal estimate of O can be calculated precisely (per equation 3.5 above). When the PSF at each point in the object cannot be analytically modelled, minimizing ϵ is achieved by semi-blindly varying the model parameters and evaluating the change in ϵ. This blind-deconvolution technique is implemented by using an iterative gradient descent algorithm (Jost et al., 2015; Chambolle and Pock, 2016):

$$\mu_{i+1} = \mu_i - \tau \nabla \epsilon(\mu_i) \tag{3.11}$$

Where μ_i is a given parameter (such as the object fluorescence or absorption at a point) taken at the i^{th} iteration, and τ provides a convergence rate over a given time. Gradient descent is particularly attractive as it can be parallelized to optimize efficiently over the full parameter space (Paudel, 2015). This provides an effective method for estimating the object, limited somewhat by convergence issues: any μ_i

that generates a local minima in ϵ acts as a possible estimate of the object. As such, having a precise estimate of the PSF and a good initial estimate of the object dramatically improves performance (Shain et al., 2017c). To obtain a model that accoutns for the intensity of the object outside the scan range, we return to the static-illumination EDOF implementation and describe the object as a three-layer structure. One layer is a mostly uniform illumination source that is generated by significantly defocused parts of the object (such as the deep brain tissue); this is modelled as a constant offset (L_0). Another layer is a network of partially defocused absorbing structures; this is modelled as having a large-width gaussian PSF (GPSF) applied to the absorbing blood vessels (D^2_{abs}), approximating strong defocus. The final layer is the object structure within the scan range; this is modelled by the EPSF described above applied to both fluorescing (S^2_{fl}) and absorbing (S^2_{abs}) cells within the scan range. Combining the layers into a single expression yields a dual fluorescence-absorption (DFA) reconstruction for minimizing the metric:

$$\epsilon = ||I - (L_0 - D^2_{abs} * GPSF + (S^2_{fl} - S^2_{abs}) * EPSF)||^2 \tag{3.12}$$

Where the $*$ operator indicates convolution. Applying the DFA reconstruction to live images of the motor cortex region of mouse brain yields significantly better contrast than the open-loop Weiner deconvolution method implemented above, as seen in figure 3·10. Moreover, by parametrizing the object in terms of both fluorescence and absorbing strucutres we obtain a representation of the neural structure and the vascular structure with a single optimization. While the neural structure is typically the focus of functional fluorescent imaging, obtaining a simultaneous representation of both structures could allow for improved probing of the neuro-vascular interactions of interest (Christie et al., 2017), without requiring additional physical

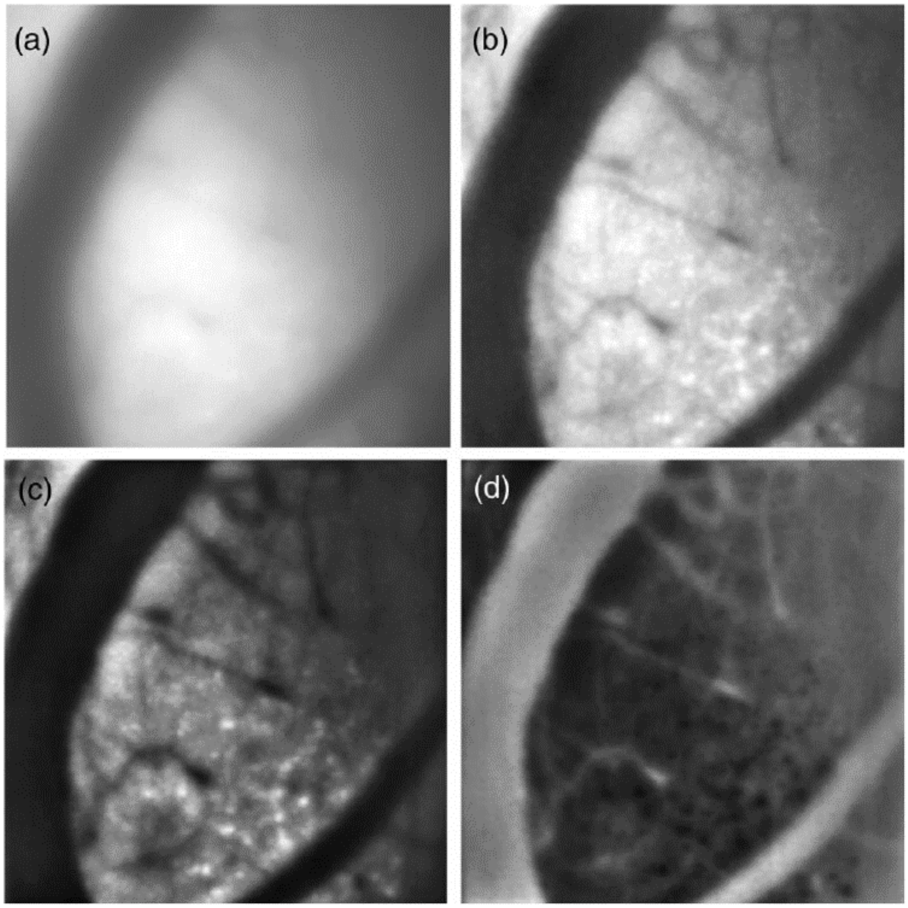

Figure 3·10: Time projection of mouse motor cortex taken with EDOF microscope; FOV $\approx 250\ \mu$m. a) raw EDOF images, b) open-loop deconvolution, c,d) fluorescence and absorbing structures using DFA deconvolution.

or computational modifications to the imaging system.

One point of note is that the object structure in equation 3.12 (described by D^2_{abs}, S_{fl}, and S_{abs}) is implemented as a parameter-squared representation, making the equation appear non-linear in the parameters. In fact, the system is still linear with respect to these squared parameters, and indeed one could replace these parameters by non-squared versions that directly represent the fluorescence or absorption of the object. Nevertheless, we obtain two advantages by describing the object with respect to squared parameters. First, it ensures positivity of the underlying values, forcing the absorbing parameters to represent reduction of intensity and the fluorescent parameters to represent increases of intensity. Second, by parametrizing the object in this manner, we promote sparse solutions upon implementing a gradient descent algorithm: as the parameter values increase they have more of an effect on the metric, favoring a solution μ_i of sparse bright objects over dense weak ones. This allows us to apply our information about the neural structure of the brain - that it is composed of discrete, sparse cells - without requiring additional constraints such as L_1 minimization (Chambolle and Pock, 2016). If we recall that the squared values of the parameters are the ones with physical meaning, we find that the deconvolution method results in a linear (and therefore quantitative) estimate of the object (Shain et al., 2017c).

Chapter 4

Compressive Linear Systems with Constraints

4.1 Matched-Filter Compressive Imaging (MFCI) Flow Cytometry

As a limiting case of mathematical complexity, we consider the case where minimal infromation from the object is acquired. Specifically, we investigate high-throughput label-free flow cytometry. Flow cytometry is used to distinguish particle types; this can be done through chemical markers with fluorescence cytometry (Wojcik and Dobrucki, 2008; Futamura et al., 2015) or geometrical structure with imaging cytometry (Blasi et al., 2016; Lei et al., 2016). Flow cytometry is used primarily for disease identification in medicine (Smith et al., 2016; Alix-Panabières and Pantel, 2013), as well as impurity detection and quality control in a variety of industries (Leme et al., 2012; Mathaes et al., 2013). Both fluorescence and imaging cytometry have their individual drawbacks that apply across the various applications: fluorescence cytometry requires the introduction of a fluorophore that can be damaging to the sample, and imaging cytometry is limited to camera acquisition rates. There is therefore a strong motivation to develop high-speed label-free cytometry, wherein the wide-field image of the particle is reformulated as a handful of critical data points that fully describe the sample.

We obtain high-speed label-free cytometry by applying a spatial filter in the fourier plane (Pasternack et al., 2008; Zhou et al., 2015) of the microscope (Fig. 4·1). The filter separates the light scattered by the particle at different spatial frequencies by tilting the light from different parts of the pupil plane into distinct high-speed detectors in the image plane, providing a form of compressed imaging (Zhou et al., 2015). For mutually incoherent regions of the field-of-view, the scatter patterns add independently on the detector. The relationship between the number of particles of a given population and the toal scattering intensity is therefore a linear one (Shain et al., 2017a), and this implementation of matched-filter compressive imaging (MFCI) flow cytometry can be described by a linear equation:

$$I_c(t) = \sum_i T_{ci} n_i(t) \tag{4.1}$$

Where $n_i(t)$ is the number of particles of the i^{th} population passing through the measurable FOV as a function of time, $I_c(t)$ is the corresponding intensity on detector c, and T_{ci} is the intensity transfer matrix (similar to the PSF in equation 3.2) connecting the scattering intensity of the particles to the signal on the detectors. For a given filter pattern, each population will have a specifc intensity map to the four quadrant detectors. This pattern can be tuned for a particular application to optimally identify a set of desired populations in a given mixture - in other words, a matched filter.

4.2 Implementation of MFCI Flow Cytometer

We use a wide-field microscope configuration, modified to include a Boston Micromachines Corp (BMC) Hex-337 tip-tilt-piston deformable mirror (TTP-DM) similar to the Iris AO PTT111 (Copeland et al., 2016). The TTP-DM is placed in a pupil-conjugate plane to implement the spatial filter. A Thorlabs 625nm LED is used for trans-illumination, and a 20x 0.46 NA Olympus objective is used to magnify the cells. A SensL high-speed quadrant detector is used to detect four distinct signals from light redirected into four quadrants in the image plane, and a Thorlabs GiGE Vision camera was placed in a conjugate-image plane to verify the separation in the image plane of the different spatial frequencies. Flowing particles are provided by a syringe pump to a lab-build microfluidic flow channel placed in the focal plane of the MFCI system. A schematic of the setup is given in figure 4·1.

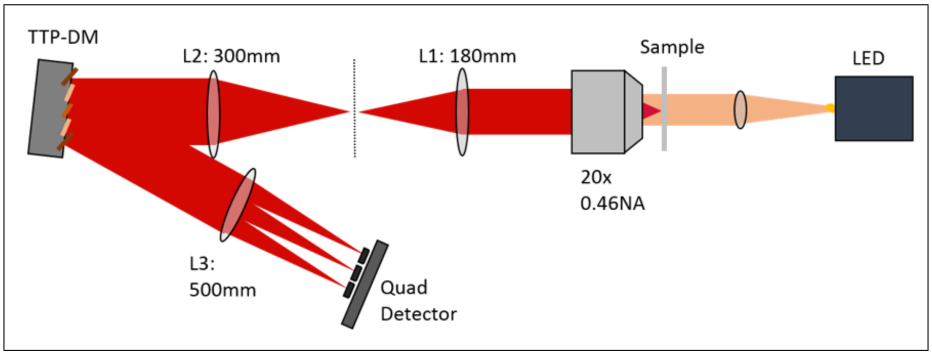

Figure 4·1: Schematic of MFCI Flow Cytometer

To test the success of our cytometry method, we investigated 4μm fluorescent beads, yeast bacteria, and Bascillus Cerus bacteria (Carolina Biological Supply) as a good representative of biological mixtures. Each particle has a unique scattering structure, depending on its symmetries and index variations, as seen in the wide-field camera images of the different objects (Fig. 4·2a-c). Moreover, each particle has a scattering pattern in the pupil plane that is invariant to the lateral position of the object: objects with low-frequency structures (such as the 4μm beads) result in light being deflected at a small angle, whereas objects with fine details (such as yeast and Bascillus Cerus) cause light to scatter at higher angles (Fig. 4·2d-f).

We verified that the signal generated by a given particle in each detector remains

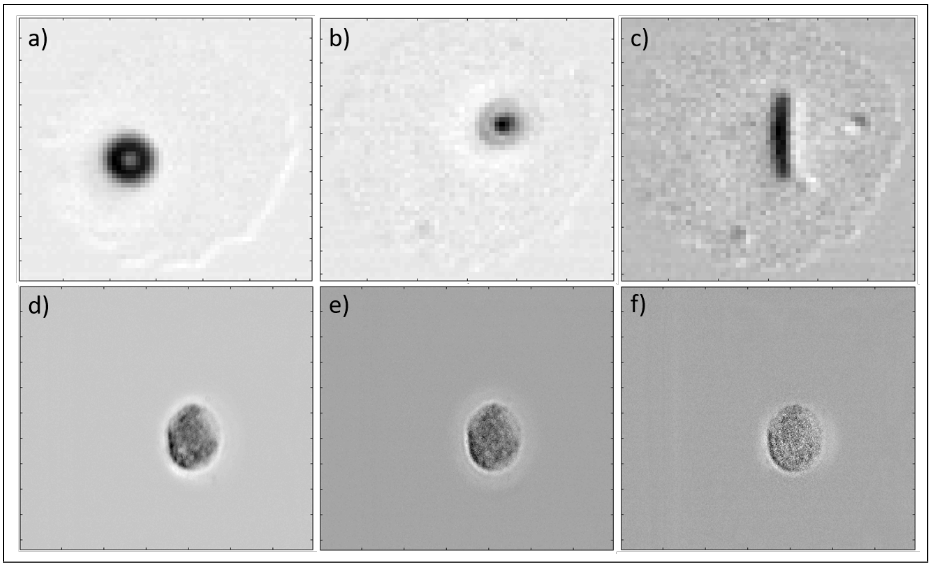

Figure 4·2: Normalized images of beads, yeast, and bascillus cerus taken in image and pupil planes. A net intensity drop is consistantly seen in all pupil plane images where the ballistic light is reduced due to scattering. For the 4μm bead (left), this light is scattered into a ring about the ballistic component; for the yeast bacteria (center), the light is scattered farther out due to the finer structure of the bacteria cell; for the bascillus cerus bacteria (right), there is increased scattering along the thin axis of the bacteria relative to the long axis, due to the asymmetry of the bacteria geometry.

constant as the particle moves across the FOV, and that different particles of the same population (and therefore the same geometry) have the same signal, as expected (Fig. 4·3). Moreover, the scattering signature of the populations were distinguishable in each channel, as shown for the beads and yeast in figure 4·4. To ensure accurate comparison of the scattering strength across channels, signals were normalized by subtracting the background intensity (taken as the median of the channel signal: $B_c = median(I_c)$) and dividing by that intensity in each channel. This represents the relative change δI in intensity for each channel:

$$\delta I_c = \frac{I_c - B_c}{B_c} \tag{4.2}$$

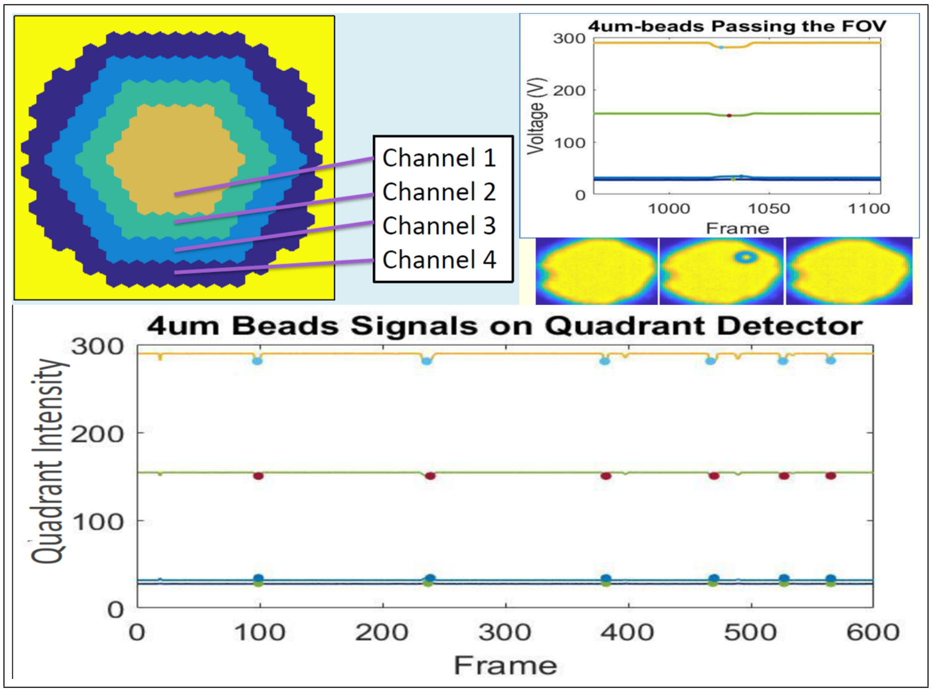

Figure 4·3: Example of Bead flowing past detector for a specific DM pattern. As the bead passes the FOV, the intensity in each channel is deflected (either increasing or decreasing) as light is scattered away from or into the corresponding spatial frequencies

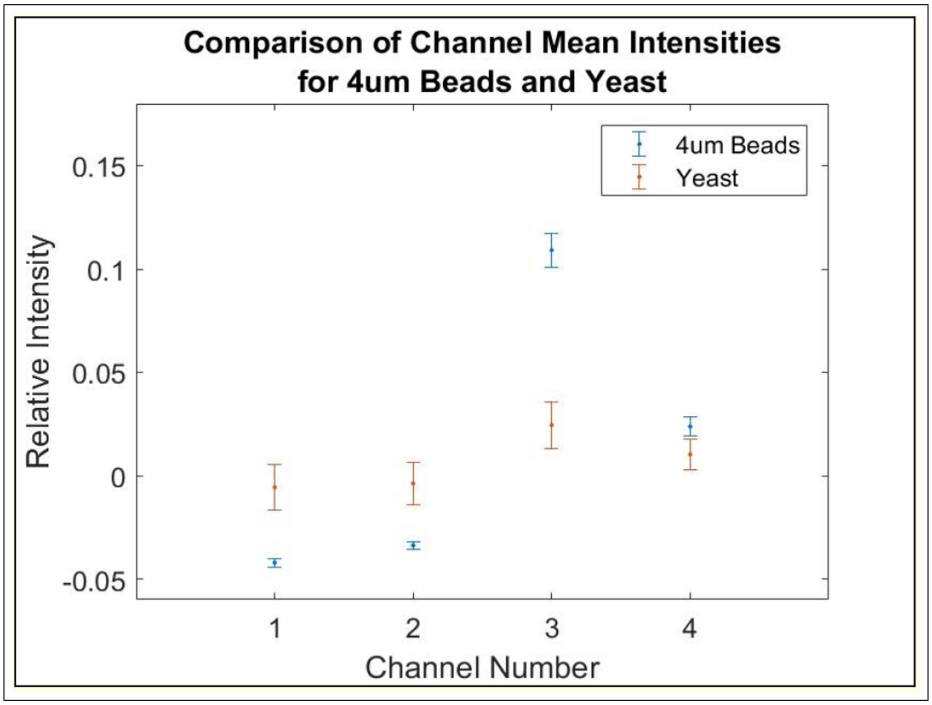

Figure 4·4: Average output signals $< \delta I_c >$ of 4μm diameter beads and yeast bacteria flowing past MFCI flow cytometer. Filter applied to separate signals is shown in figure 4·3. Clear separation between the beads and the yeast signals are visible in each of the four channels.

4.3 Linear Inversion through Machine Learning

Equation 4.1 is a linear transfer equation, just like equation 2.2 and 3.2. It would be tempting to apply the same division-style inverse as equations 2.3 and 3.4 (or equation 3.5). In equation 4.1, however, there is a critical underlying distinction: the number of particles n_i that are transfered to the intensity at the detector is a positive discrete integer for each population. This constraint cannot be implemented through division or pseudo-inversion techniques, and would be difficult to implement with closed-loop optimization due to noise fluctuations. An entirely different solution method is necessary.

To invert the linear equation 4.1 defining the MFCI, we implemented a machine-learning (ML) algorithm (such as nearest-neighbor clustering, or a neural-network) to find the optimal solution. These algorithms have found wide-spread use in image data partitioning and feature/object identification (Sinha et al., 2017; Lin et al., 2017; Steinvall et al., 2017), and have been widely demonstrated to be robust to noise and population variations given a sufficiently sized dataset. While ML algorithms can be applied to linear and non-linear problems, a critical simplification to our ML algorithm arises from the linear nature of equation 4.1 demonstrated in figure 4·5: the training data need only include instances of single isolated particles from each population. Given such a training set, we can extrapolate our ML algorithm to account for any arbitrary combination of cells by scaling the expected signals and summing accordingly. This is a unique feature to linear systems that in general is lacking in ML applications. On a practical level, this drastically simplifies the traning process, as well as the ability for transfer learning of a given population signature to a different cell mixture. Preliminary data suggests this is a viable approach, however a more thorough analysis is needed to demonstrate the success of supervised machine learning to cluster the populations in an MFCI flow cytometer.

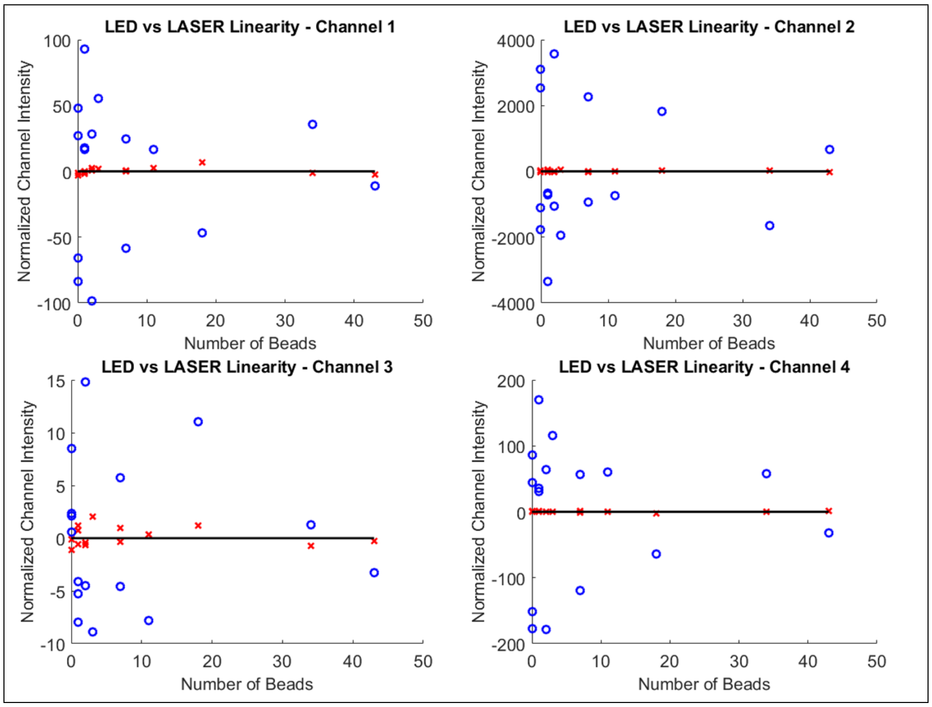

Figure 4·5: Linearity of LED illumination vs. Laser Illumination: groups of 2μm beads placed in the FOV and imaged with both a laser and an LED source. Intensity in each channel is recorded, after subtracting a line of best-fit as a linear assumption. For laser illumination (blue circles) in each channel, the intensity varied wildly depending on the number of beads; whereas with LED illumination (red x's), the intensity was relatively constant even with significant changes in particle count.

As a final point, we note that while the detector response is linear with respect to the cell population, it is highly non-linear with respect to the filter shape on the DM. Different patterns will identify specific populations from a given mixture, and there is no clear analytic prediction that can be used to design the filter for optimal detection. Such optimization would be especially useful for applications such as cancer detection or water contamination, in which the particles that must be detected are (hopefully) rare. Fortunately, ML algorithms are effective for non-linear applications as well, and the ML architecture set in place for particle identification can be easily modified to incorporate an ML pattern optimization schemel. Such an optimization algorithm is the subject of future work on the MFCI flow cytometer project.

Chapter 5

Conclusions

5.1 A General Linear Microscopy Framework

Information about an object can be recovered by a microscope through the effect of the object on the electromagnetic field. The greater the gap between the minimal object description and the information provided by the microscope, the more powerful the mathematical techniques for fully recovering the object. Fortunately, since much of optics depends on linear transfer equations, more powerful mathematical techniques are readily available.

Seeing through rock with an S-MPM microscope implementing MPO imaging required only the simplest manifestation of linear mathematics to reconstruct the object: most of the necessary information was extracted by the microscope directly, after physically correcting the light paths with a DM. For dynamic volumetric objects, part of the object was recovered through focal scanning with a DM. However, the remainder of the information required the more advanced regularized deconvolution methods as the linear equation was ill-defined for specific frequencies. For large objects extending beyond the expanded depth-of-field, regularized deconvolution was insufficient and a closed-loop multi-layer model was required. With MFCI flow cytometry, a DM supplied the minimum necessary information through compressed spatial filtering. The compression of the object geometry, as well as the constraints on the object parameters, suggested that even a closed-loop deconvolutin algorithm would be unable to recover the cell populations at a given moment. Instead, the more powerful machine-learning techniques are necessary to obtain accurate identification of the sample.

The key observation is that as the requirements for extracting the object information change, both the physical microscope and the extraction algorithm must respond accordingly. We can write a sort of pseudo-equation that describes the situations in which one can fullly recover the object:

$$P(1 + A) \subset O \tag{5.1}$$

The information supplied by the physical microscope (P), modulated by the information supplied by the inversion algorithm (A), must contain the necessary object information (O). The microscope technique can be tuned for the problem at hand by using SLM's to maximize the information available, and the mathematical recovery algorithm must be chosen by exploiting the linear nature of optics to fill in the information gap. As more information is needed under harsher physical constraints, both the physical microscope and the computational recovery must be refined. This balance between experimental and theoretical enhancements is found throughout physics and science in general, and as we see in the above examples, they should be considered in tandem. Ideally one could express both the microscope and the algorithm in a single framework that would allow easy identification of the systems capable of recovering a given sample, optimizing not just a given microscope system for a given application but instead the whole field of microscopy. This thesis provides a small potential step towards such an architecture.

Appendix A

Derivation of the Classical Microscope Propagator

A.1 The Origin of Plane Waves

A.1.1 Plane Wave Decomposition

Any continuous function of real space can be written as a (potentially infinite) composition of plane waves. This is commonly known as a Fourier decomposition (Jackson, 1999) and is formulated through:

$$\vec{\mathcal{E}}(\vec{k}_\perp) = \int e^{-i2\pi\vec{k}_\perp\cdot\vec{\rho}_0}\vec{E}(\vec{\rho}_0) \tag{A.1}$$

Where the fourier modes $\vec{\mathcal{E}}$ are eigenfunctions of the wave equation 1.2. Breaking the propagation vector $\vec{k}$ into $\vec{k} = \vec{k}_\perp + \vec{k}_z$, an arbitrary plane wave can be re-written as propagating a distance D along the $\hat{z}$ direction with a temporal frequency w, axial spatial frequency $|\vec{k}_z| = \sqrt{k^2 - |\vec{k}_\perp|^2}$, and eigenvalue $e^{i2\pi(k_zD-wD/c)}$. Summing over each plane wave multiplied by its respective eigenvalue gives the total electic field in the Fourier basis as an integral over the transformed plane-waves. Since the two vector components of the field sum independently, we suppress the vector nature for now unless otherwise specified. Taking an inverse Fourier-transform gives the field in the final plane (as seen in figure A·1):

$$E(\vec{\rho}, D) = \int\int e^{i2\pi\vec{k}_\perp\cdot\vec{\rho}} e^{\pm i2\pi D\sqrt{k^2-|\vec{k}_\perp|^2}} e^{-i2\pi\vec{k}_\perp\cdot\vec{\rho}_0} E(\vec{\rho}_0, 0) d^2\vec{\rho}_0 d^2\vec{k}_z \tag{A.2}$$

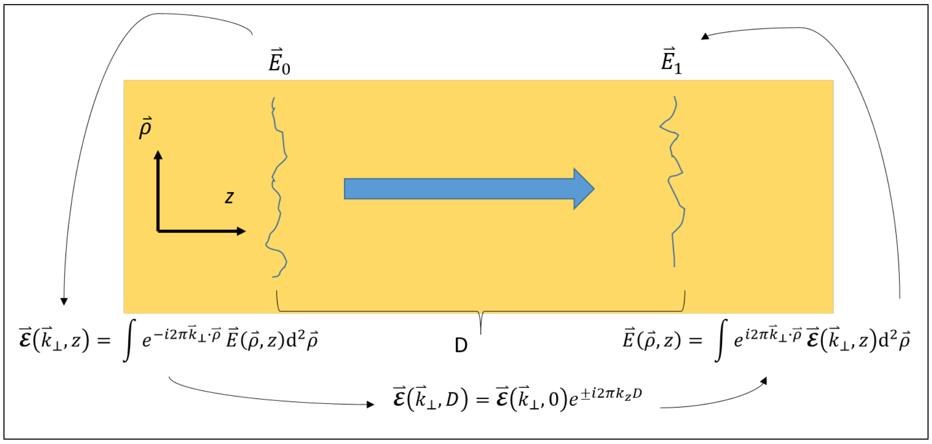
$\vec{E}_0$
$\vec{E}_1$
$\vec{\rho}$
z
D
$\vec{\mathcal{E}}(\vec{k}_\perp, z) = \int e^{-i2\pi\vec{k}_\perp\cdot\vec{\rho}}\,\vec{E}(\vec{\rho}, z)\mathrm{d}^2\vec{\rho}$
$\vec{E}(\vec{\rho}, z) = \int e^{i2\pi\vec{k}_\perp\cdot\vec{\rho}}\,\vec{\mathcal{E}}(\vec{k}_\perp, z)\mathrm{d}^2\vec{\rho}$
$\vec{\mathcal{E}}(\vec{k}_\perp, D) = \vec{\mathcal{E}}(\vec{k}_\perp, 0)e^{\pm i2\pi k_z D}$

Figure A·1: Propagation of light through a homogeneous medium.

This can be re-written to remove the intermediate Fourier transform, leaving the solution in terms of only the initial and final co-ordinates:

$$E(\vec{\rho}, D) = -ik\int \frac{D}{\rho_0^2 + D^2} e^{i2\pi k\sqrt{\rho_0^2+D^2}} \left(1 + \frac{i}{2\pi k\sqrt{\rho_0^2 + D^2}}\right) E(\vec{\rho}_0, 0) d^2\vec{\rho}_0 d^2 \tag{A.3}$$

While equation A.3, called the Rayleigh-Sommerfeld diffraction integral, is an exact description of free-space light propagation, it is extremely difficult and mostly unnecessary to solve for the cases of relevance (Mertz, 2010). Of note is the fact that for sufficiently high lateral spatial frequencies, the exponential becomes a real decaying function and its contribution to the integral becomes negligible for classical microscopes (the origin of the so-called "Diffraction Limit"). This suggests that we should limit our integration over lateral spatial frequencies to those of finite value. Indeed, we will take the paraxial approximation in which we assume the light is mostly going straight ($|k_\perp| << k$), and therefore $k_z = \sqrt{k^2 - |\vec{k}_\perp|^2} \approx k(1 - \frac{|\vec{k}_\perp|^2}{2k^2})$. This appoximation vastly simplifies the form of the propagtator, as seen below (A.1.3), and is valid for all the microscope systems discussed here.

A.1.2 Making an Image

When there are discontinuties in the refractive index, equation A.2 no longer applies. However, if the disruption in the refractive index is short, such as light passing through a thin film, we can approximate the transmitted field as having a local phase shift depending on the local index variation:

$$\vec{E}(\vec{\rho}, dT) = \vec{E}(\vec{\rho}, 0)e^{i2\pi\frac{dT}{\lambda}\Delta n(\vec{\rho})} \tag{A.4}$$

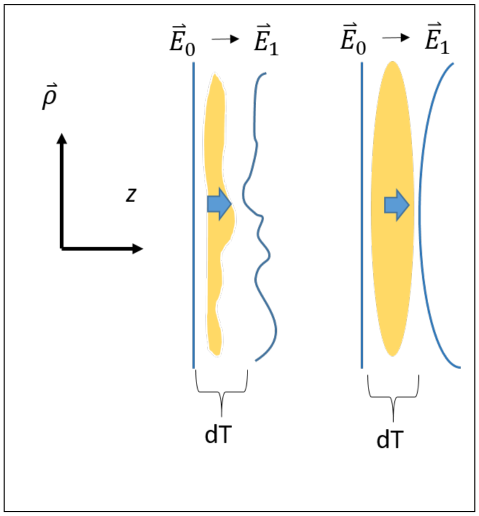

Figure A·2: Propagation of light through a thin film for an arbitrary wave plate and for a quadratic phase .

When the phase variation takes the form of a 2D parabola (Fig. A·2), it acts as a lens of focal length f. The effect can be characterized as imparting an additional curvature $\kappa = \frac{1}{f}$ to the phase of the electric field. If we describe the input field E_0

as having its own well-defined curvature κ_0, such as the electric field generated by a point source or Huygens wavelet (Jackson, 1999), the effect of the parabolic thin film is to simply sum the curvature linearly:

$$\begin{aligned}\vec{E}(\vec{\rho}, dT) &= \vec{E}(\vec{\rho}, 0)e^{-i\pi\frac{k}{f}|\vec{\rho}|^2} \\ &= \vec{E}(\vec{\rho}, 0)e^{-i\pi k\kappa_L|\vec{\rho}|^2} \\ &= \vec{E}_0 e^{-i\pi k\kappa_i|\vec{\rho}|^2} e^{-i\pi k\kappa_L|\vec{\rho}|^2} \\ &= \vec{E}_0 e^{-i\pi k\kappa_f|\vec{\rho}|^2}\end{aligned} \tag{A.5}$$

Where $\kappa_f = \kappa_0 + \kappa_L$. For sufficient positive curvature, this forces the field back to a point - the defining feature of a lens. Re-writing the curvature of the input and output fields in terms of the convergence points $d_0 = \frac{1}{\kappa_0}$ and $d_f = \frac{1}{\kappa_f}$ results in the classic thin lens equation:

$$\frac{1}{d_0} + \frac{1}{f} = \frac{1}{d_f} \tag{A.6}$$

A.1.3 The Classic Microscope

When a plane wave is incident on the lens, we can treat the plane wave as if it has zero curvature ($d_0 = \infty$), bringing any plane wave into focus at $d_f = f$. Since the tilt of the field is unaffected by the lens, a plane wave incident at an angle θ is brought into focus at a distance $|\vec{\rho}| = f \sin(\theta)$ from the lens axis. This unique feature of a lens to map planewaves to points (and points to planewaves) implies a conjugate relationship between the position of a light wave and the angle at which it propagates (Fig. A·3). Indeed, for the paraxial approximation mentioned above (section A.1.1) we can derive a Fourier transform relationship between the electromagnetic field at

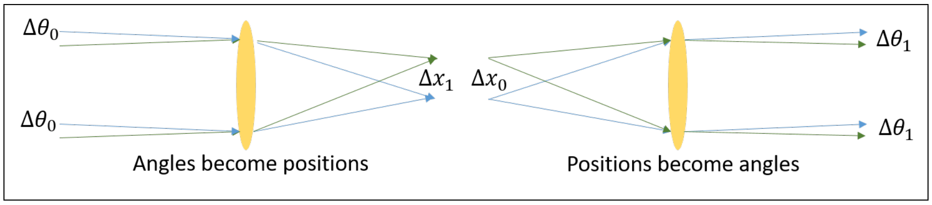

Figure A·3: Fourier-conjugate nature of positions and angles between one focal plane of a lens and the other.

the initial focal plane and the field at the final focal plane. Following the work of (Mertz, 2010), we obtain:

$$\vec{E}(\vec{\rho_1}) = -i\frac{k}{f}e^{i4\pi kf}\int e^{-i2\pi\frac{k}{f}\vec{\rho}_1\cdot\vec{\rho}_0}\vec{E}(\vec{\rho_0})d^2\vec{\rho_0} \tag{A.7}$$

Since we also identify the input field with a plane-wave representation, we identify the field at a given co-ordinate in the output plane with the laterial spatial frequency at the input plane: $k_\perp = \frac{2\pi}{\lambda f}\rho$. The field at one focal plane of a lens is precisely the Fourier transform of the field at the other focal plane (within the paraxial approximation). If we then place a second lens a distance $d = f_1 + f_2$ after the first (Fig. A·4), the result chains together two Fourier transforms:

$$\begin{aligned}
\vec{E}_I(\vec{\rho_I}) &= -\frac{k^2}{f_1 f_0}e^{i4\pi k(f_1+f_0)}\iint e^{-i2\pi\frac{k}{f}\vec{\rho}_1\cdot\vec{\rho}_P}P(\vec{\rho}_P)e^{-i2\pi\frac{k}{f}\vec{\rho}_P\cdot\vec{\rho}_P}\vec{E}(\vec{\rho_0})d^2\vec{\rho_P}d^2\vec{\rho_0} \\
&= -\frac{k^2}{f_1 f_0}e^{i4\pi k(f_1+f_0)}\int\Big[\int e^{-i2\pi\frac{k}{f}\vec{\rho}_1\cdot\vec{\rho}_P}P(\vec{\rho}_P)e^{-i2\pi\frac{k}{f}\vec{\rho}_P\cdot\vec{\rho}_P}d\vec{\rho_P}\Big]\vec{E}(\vec{\rho_0})d^2\vec{\rho_0} \\
&\approx -\frac{k^2}{f_1 f_0}e^{i4\pi k(f_1+f_0)}\int\delta\big(\frac{1}{M}\rho_1 - \rho_0\big)\vec{E}(\vec{\rho_0})d^2\vec{\rho_0} \\
&= -\frac{k^2}{f_1 f_0}e^{i4\pi k(f_1+f_0)}\vec{E}_O\big(-\frac{f_0}{f_1}\vec{\rho}_I\big)
\end{aligned} \tag{A.8}$$

Where the magnification is $M = -\frac{f_1}{f_0}$, and the ideal pupil function $P(\vec{\rho}_P) = 1$;

that is, the light is perfectly transformed by the two successive fourier transforms. The result of equations A.8 is a flipped and rescaled version of the input field to the first lens appearing at the output focal plane of the second lens. Whereas a single lens mapped the electromagnetic intensity at one plane to another (per equation A.6), the phases in the new field were not identically preserved. With a 4f system, the propagator function in equation A.8 approximates a delta-function, allowing us to reproduce any electromagnetic field at another plane magnified by a factor $M = \frac{f_2}{f_1}$. In fact, taking into account the finite radiation frequency, we can better express the microscope in terms of its coherent transfer function (CTF), defined as the transfer function of the fourier components. For a 4f microscope, the CTF is identical to the pupil function P (Mertz, 2010) In the fourier domain, this is easily expressed by having the pupil function have a finite cutoff:

$$P(\vec{\rho}_P) = \begin{cases} 1 & \rho_P < \frac{f}{k}\Delta k \\ 0 & \rho_P > \frac{f}{k}\Delta k \end{cases} \tag{A.9}$$

Where $\Delta k = \frac{2NA}{\lambda}$ defines the passband of the microscope. Identifying the pupil position $\vec{\rho}_P$ with the fourier mode of the field $\vec{k}_\perp = \frac{k}{f}\vec{\rho}_P$ allows us to write the microscope in terms of how it transmitts spatial frequencies:

$$\mathcal{E}_I(\vec{k}_\perp) = P(\vec{k}_\perp) \cdot \mathcal{E}_O(\vec{k}_\perp) \tag{A.10}$$

Where the finite cutoff defined by Δk creates the diffraction limit. As a result, we express the field at the image through:

$$\vec{E}_I(\vec{\rho_I}) = \int CSF(\frac{1}{M}\vec{\rho}_I, \vec{\rho}_0)\vec{E}_O(\vec{\rho}_O)d^2\vec{\rho}_O \tag{A.11}$$

Where the coherent spread function (CSF) is the Fourier transform of the CTF. This defines a classical microscope as seen in Fig. A·4, and is the basis of optical microscopy (equation 1.7 in section 1.1).

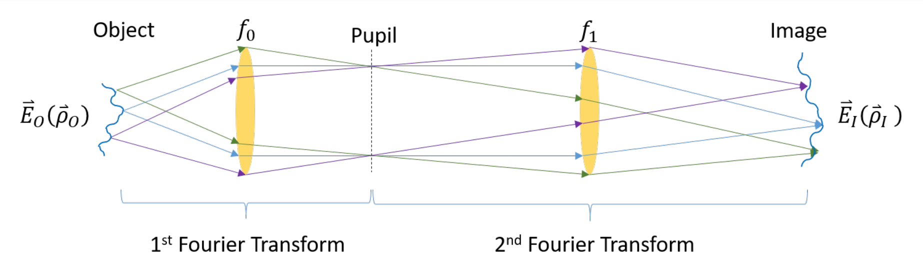
Object
f_0
Pupil
f_1
Image
$\vec{E}_O(\vec{\rho}_O)$
$\vec{E}_I(\vec{\rho}_I)$
1st Fourier Transform
2nd Fourier Transform

Figure A·4: Classical Microscope System

Appendix B

Optical Characterization of Porous Rock

Porous rock is a highly scattering medium when filled with air, water, or even oil. This is due to both the fractal nature of the pore structure and the large refractive index of the rock itself. As such, a variety of metrics are necessary in order to properly characterize how well one can image through a thin rock section. Many of the physical aspects of limestones and other oil-well rocks have been well described by the literature, however the optical characteristics of the rock were lacking. We therefore investigated the two parameters most indicative of our ability to recreate a focal spot deep in the rock: the Transport Mean-Free-Path (l^*) and the Sample Bandwidth ($\Delta\nu_s$). These parameters allow us to estimate the usable field-of-view and our expected signal-to-noise ratio at a given point in the rock.

B.1 Transport Mean-Free-Path

When light initially enters a scattering medium, it is dominantly ballistic: most of the photons are ballistic, and any aberrations or weak scattering can be fully corrected using spatial light modulation techniques (Li et al., 2015). However, as light continues into the sample the ballistic component of the light decays exponentially, as determined by the scattering length l_s. As a result, the corrlations between the transmission to different points in the sample decrease (Berkovits and Feng, 1994), reducing the field-of-view (see also section2.2). At a certain thickness into the sam-

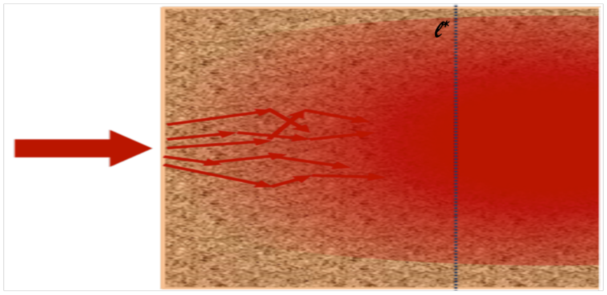

Figure B·1: Diagram of light travelling through a scattering medium. Initially the light retains its directionality, but by l^* (dotted line) the light is now diffusing evenly throughout the sample.

ple, light can be approximated as diffusing through the medium (Ishimaru, 1978), propagating equally forwards and backwards through the rock (Fig. B·1). This characteristic distance defines the Transport Mean Free Path (l^*); beyond this thickness, phase information of the incoming beam is lost. At a thickness of l^* the corrected FOV is reduced to a diffraction limited spot (Fig. 2·4). l^* therefore provides important information on how well we can image inside a particular sample using the S-MPM technique.

In order to measure l^*, we followed the work by Genack (Genack, 1987) where transmission through a thick non-absorbing diffusive slab can be approximated as:

$$T(L) = \frac{5}{3}\frac{l^*}{L} \tag{B.1}$$

Here, $T = \frac{I_{trans}}{I_{in}}$ is the normalized transmission ratio and L is the sample thickness. To estimate l^*, we used an integrating sphere to collect the full transmitted light for a given thickness and solved equation B.1 for l^* in terms of the transmission ratio and sample thickness. While the specific value of l^* varied significanly for different rock samples, ranging from tens to hundreds of microns, we were able to verify that l^* increased with as both the index mismatch and the porosity of the medium decreased, in both cases resulting from increased homogeneity of the rock. A full examination of the transport mean-free-path of rock was beyond the scope of our research.

B.2 Sample Bandwidth and Diffusion Coefficient

The S-MPM microscope in section 2.2 relies on coherent optimization of speckle grains to produce an optimized focal point, enhanced above the average intensity by $E = \frac{I_{opt}}{I_{avg}}$. A key requirement to successfully enhance the multi-photon signal required for 2.2 is the specular structure of the output light; that is, there must exist distinct spatial fluctiations that are then optimized. The light passing through the scattering medium must therefore generate a limited number of frequency modes - white light has no speckle to optimize. However, as light travels through the scattering medium, the multiply-scattered light can dwell in the medium for a significant time. This delay, called the Thouless time (τ_{Th}) causes different frequency components loose coherence and separate into distinct frequency modes (see Fig. B·2). A given sample will have a bandwidth called the Sample Bandwidth (Δv_s) where sources of shorter bandwidth $_l$ remain coherent. The sample and source bandwidths together determine the maximum enhancement obtainable with a phase modulator of N elements (Paudel et al., 2013):

$$E = \frac{\pi}{4} N \frac{\Delta v_s}{\Delta v_s + \Delta v_l} \tag{B.2}$$

To determine Δ_s for porous rock, we followed the work of ref. (Paudel et al., 2013) and controlled the bandwidth of an optical source before passing through the rock sample. We used a super-luminescent diode (SLD) to generate a large bandwidth beam. A diffraction grating spatially separated the frequency components, and a tunable slit filtered out the edges of the beam to directly tune the bandwidth. After specifying the bandwidth, the beam was redirected to focus onto the rock sample, and the diffuse light transmitted through the rock was collected on a camera (Fig. B·3). We correlated the intensity contrast of the output speckle pattern (defined as the standard devaition divided by the mean intensity) with the laser bandwidth (Paudel et al., 2013):

$$C = \sqrt{\frac{\Delta v_s}{\Delta v_s + \Delta v_l}} \tag{B.3}$$

The sample bandwidth is expected to vary with thickness as: $\Delta v_s = \frac{D}{L^2}$, so from Δv_s and the thickness we can calculate the diffusion coefficient D. Porous rock had diffusion coefficients ranging from 10^4 to 10^5 m^2/s, with larger (faster) diffusion generally occuring for lower scattering strength. For imaging water and oil flow at about 100μm deep, this resulted in a sample bandwidth of about 1-2 THz and 50THz. When used in conjunction with our femtosecond laser and Kilo-SLM, we expect an enhancement of 1 at about 200μm, beyond which point the optimization is expected to fail entirely for lack of signal. We therefore would not expect to obtain any improved imaging cabability at depths beyond 200μm without increasing the number of elements in our SLM.

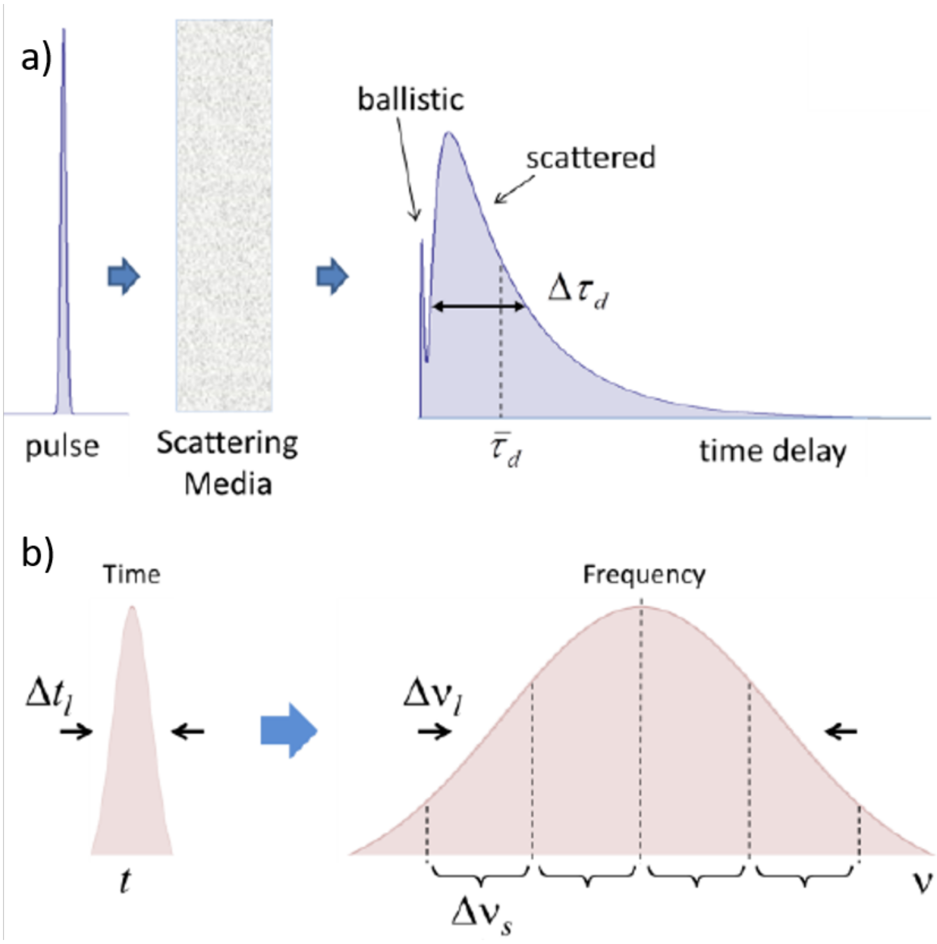
a)
pulse
Scattering Media
ballistic
scattered
$\Delta\tau_d$
$\bar{\tau}_d$
time delay
b)
Time
Δt_l
t
Frequency
$\Delta\nu_l$
$\Delta\nu_s$
ν

Figure B·2: a) Diagram of laser pulse incident on scattering media. The ballistic light exits as if there were no scattering, retaining the pulse shape. The scattered light exits after the ballistic light, and spreads significantly in time. b) Diagram of sample bandwidth. Broad pulse corresponds to a beam of finite bandwidth. For a finite bandwidth Δ_l incident on a scattering media, the spectrum is divided into blocks of width $\Delta\nu_s$ which remain coherent. The above spectrum, for example, is broken into approximately four distinct modes.

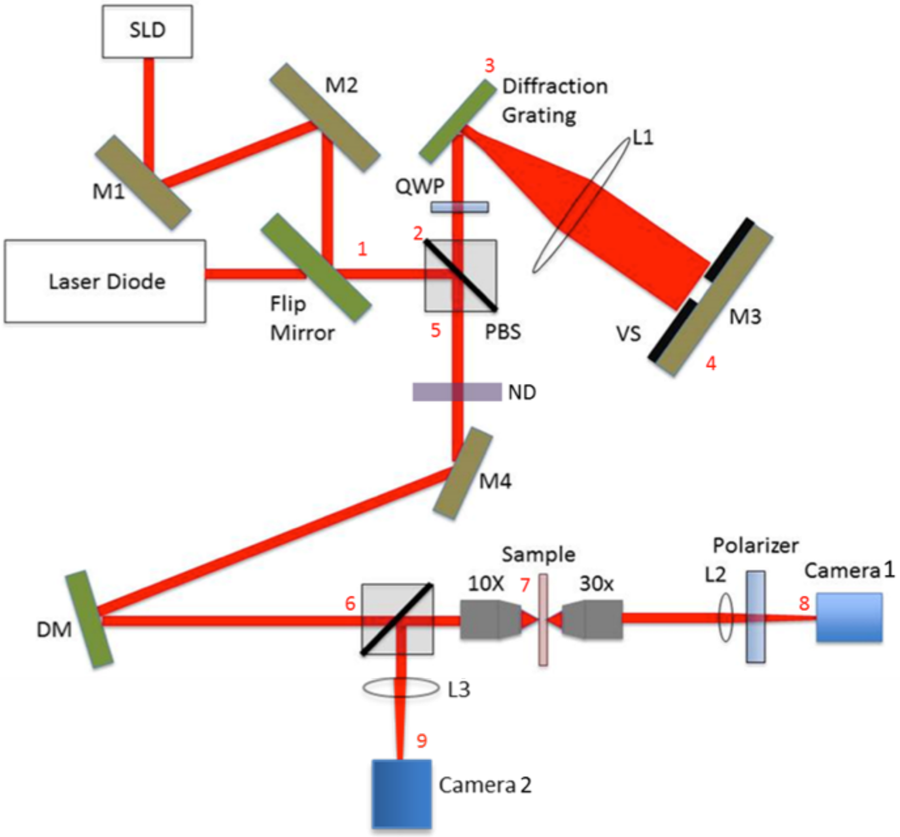
SLD
M1
M2
Laser Diode
Flip Mirror
1
2
3
Diffraction Grating
QWP
L1
PBS
5
VS
M3
4
ND
M4
DM
6
Sample
10X
7
30x
Polarizer
L2
8
Camera 1
L3
9
Camera 2

Figure B·3: Schematic of setup used to measure the sample bandwidth Δ_s. An SLD was directed onto a diffraction grating and spatially filtered with a tunable slit; from there it was recombined and redirected to the sample, and the transmitted light imaged on the camera. SLD: Super-luminescent diode, PBS: polarizing beam splitter, ND: neutral density filter, QWP: quarter wave plate, DM: deformable mirror, L: lens, M: mirror

Appendix C

Image Analysis in Low SNR environments

As we are imaging deep within the rock, we will necessarily be analyzing both high-quality and low-quality images, depending on the local thickness and scattering properties of the rock. We found that the traditional method of applying a threshold and clustering adjoining signals lead to fragmented or over-clustered data when applied to close-packed, noisy images (Fig. C·1).

C.1 Partitioning by Local Maxima

We therefore defined beads by clustering pixels according to their local maxima (Youssef, 1987). Any two pixels are deemed equivalent if one is the local maximum of the other. The local region is taken to be approximately the resolution or point-spread function (PSF) of our imaging system. Once we have partitioned the image, we then define the structures within each region. For beads (or other spherical structures) we define a Full-Diameter at Half-Max (FDHM) for each local maximum. The FDHM of each region is calculated by averaging the Full-Width at Half-Max taken from line-scans at multiple angles, each centered about the local maximum. The radius of the bead is half the FDHM. We can then define the intensity of a bead as the mean intensity of all pixels within the bead radius. Note that as we have not yet defined a threshold, every region has an associated bead structure including regions which arise from noise fluctuations. By defining the intensity through the

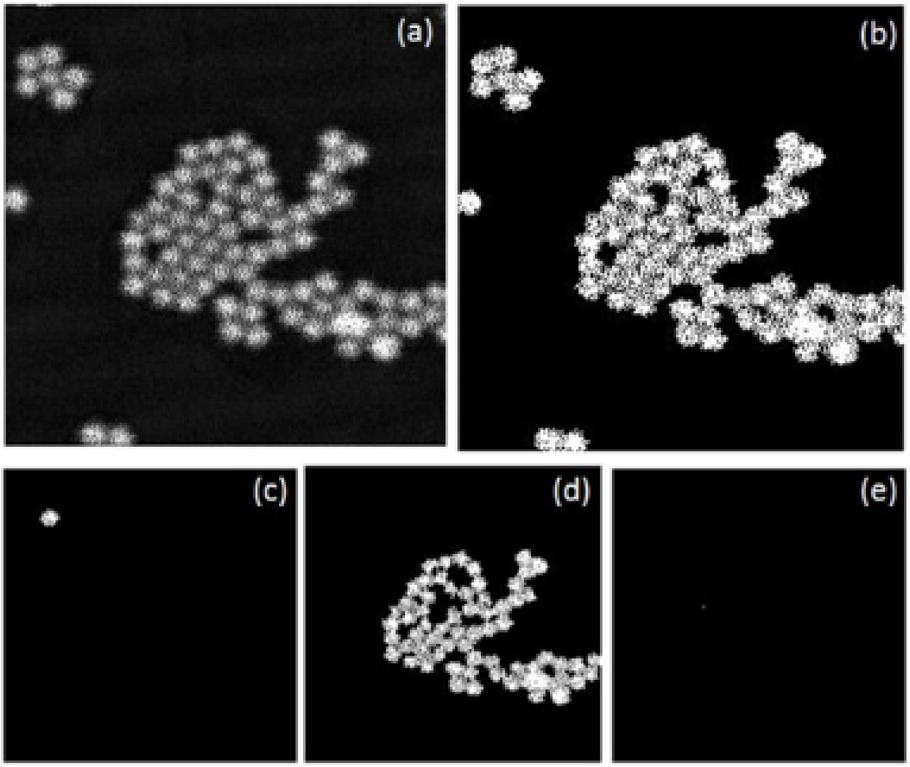

Figure C·1: Threshold and cluster method used to identify 1μm diameter beads in a 20μm x20μm image. Each pixel in the initial image (a) is defined as signal or background, creating a binary image (b). Adjacent signal pixels are combined to form a single structure, such as a bead (c). However, the algorithm may misidentify a chain of beads as a single structure (d) or isolate a few pixels (e).

FDHM, we can now see a clear separation in intensity between true bead structures that arise from imaging actual fluorescent objects and background structures that arise from noise fluctuations. The two populations are well-separated in intensity, as shown in a histogram of bead intensities. This allows for a natural definition of a threshold value for signal: by grouping the histogram data towards the local maxima, we find a natural separation point between the two populations. We can then use this threshold to remove the background structures, allowing for easy analysis of only the actual beads (Fig. C·2).

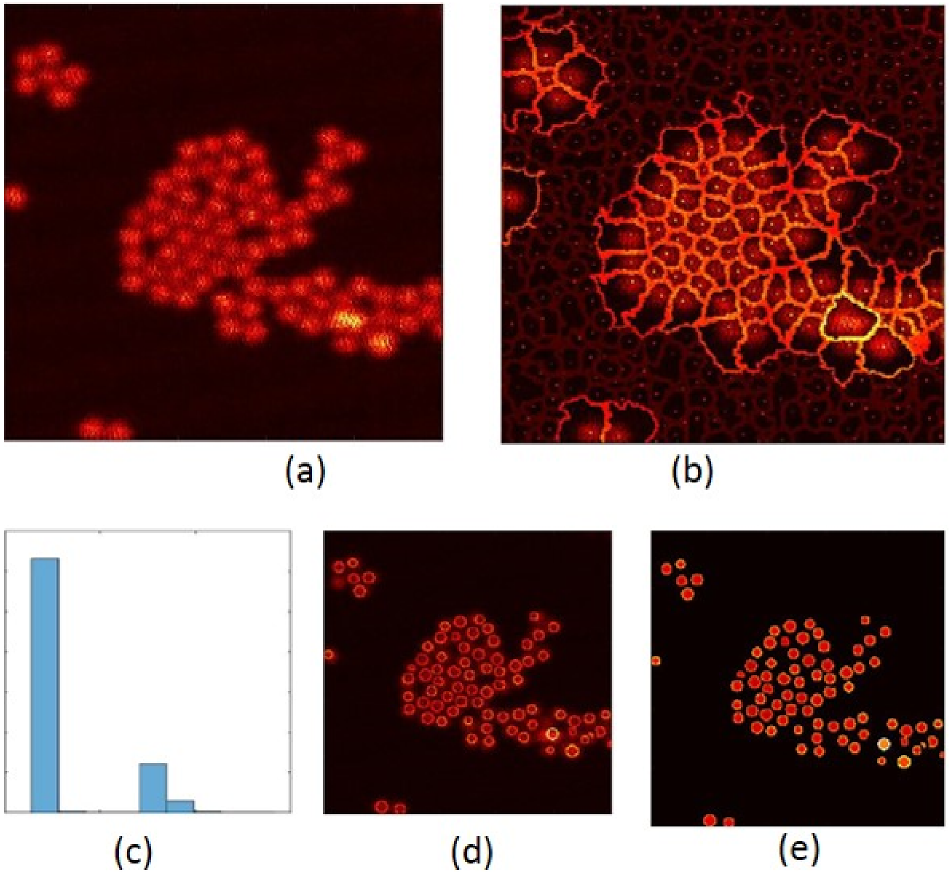

Figure C·2: Use of partitioning to identify beads. Initial image (a) is broken into local regions with local maxima (b). By taking a local measure of the intensity and plotting a histogram of the regions (c), we see regions naturally separate into background and signal. This lets us identify and quantify the bead intensities and geometries

C.2 Primary Image Metrics

To quantify the image quality of an image, we use a total of 5 metrics. The apparent resolution, contrast, and SNR apply to any image, and the enhancement and FOV are defined only for images taken after optimization. These parameters accurately characterize how the rock affects the imaging capabilities as a function of depth into the sample (Fig. 2·4), and additional parameters of potential interest are measured as well (Fig. C·3).

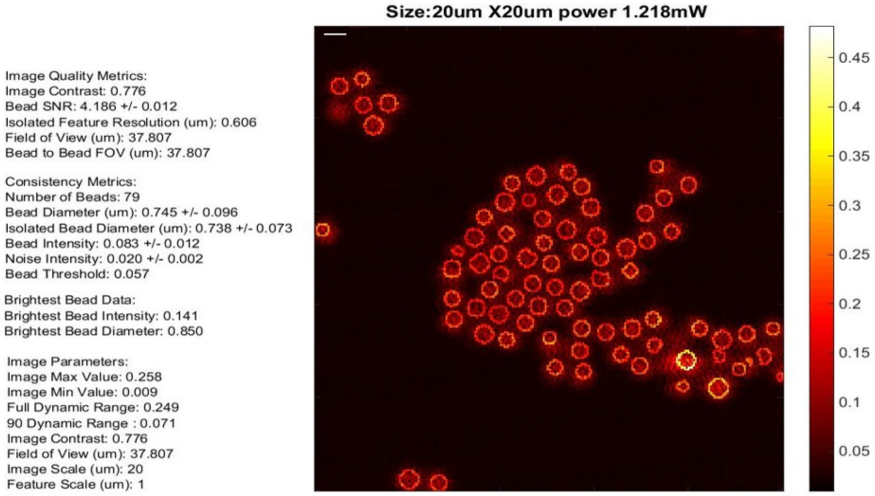

```
Image Quality Metrics:
Image Contrast: 0.776
Bead SNR: 4.186 +/- 0.012
Isolated Feature Resolution (um): 0.606
Field of View (um): 37.807
Bead to Bead FOV (um): 37.807

Consistency Metrics:
Number of Beads: 79
Bead Diameter (um): 0.745 +/- 0.096
Isolated Bead Diameter (um): 0.738 +/- 0.073
Bead Intensity: 0.083 +/- 0.012
Noise Intensity: 0.020 +/- 0.002
Bead Threshold: 0.057

Brightest Bead Data:
Brightest Bead Intensity: 0.141
Brightest Bead Diameter: 0.850

Image Parameters:
Image Max Value: 0.258
Image Min Value: 0.009
Full Dynamic Range: 0.249
90 Dynamic Range : 0.071
Image Contrast: 0.776
Field of View (um): 37.807
Image Scale (um): 20
Feature Scale (um): 1
```

Figure C·3: Output of analysis program applied to 20μm x 20μm image of 1μm diameter beads (no scattering). The structures creating signal are identified, and the relevant image metrics and parameters are recorded. Scale bar: 1μm

Resolution: We define the apparent resolution of an image as the smallest FDHM of isolated fluorescent structures (such as a single bead with no neighbors) in the image. The smaller the resolution, the higher the image quality. It is necessary to use isolated structures, as beads that are touching may generate artificially small radii, overestimating the resolution. It is important to note that we cannot measure resolution smaller than the fluorescent structure - if we image 5μm diameter beads with a 1μm Point-Spread-Function (PSF), the image would indicate a resolution of at least 5m, but no more. Since the resolution is independent of the power at the sample or the noise in the system, we can use it to compare imaging techniques, rather than only the imaging systems.

Signal-Noise Ratio: The signal-nose ratio (SNR) of an image is defined as the ratio of the intensity of the true bead structures to the background parts of the image, which are defined through the intensity histogram (Fig C·2). For a high-quality image with well-separated signal and background the ratio is easily defined. When imaging deep inside rock, however, the SNR decays to 1, and the actual value becomes sensitive to the binning of the histogram. In this limit, the contrast becomes a more useful metric of image quality.

Contrast: The contrast of an image is defined as the standard deviation of the intensity divided by the mean intensity. A higher contrast typically indicates a higher quality image: as the standard deviation is measuring the difference between the signal and background intensities, the contrast is qualitatively similar to the SNR. As we image deeper into the rock, and the SNR drops to 1, the fluctuation in intensity occur more to system noise or speckle. In this limit, we can no longer distinguish the signal and noise peaks, a higher contrast actually implies a lower quality image, as it implies more pixel-to-pixel noise (such as shot noise) relative to the signal from the fluorescence.

Enhancement: The enhancement of an optimization is defined as the ratio of the intensity of the optimized pixel after optimization to before optimization. As the optimization procedure redirects power into the optimized pixel, a high enhancement indicates a stronger optimization. As we image deeper into the rock, the maximum enhancement we can obtain initially increases as we correct for more scattering. However, as we go deeper into the rock, the number of independent frequency modes increases, limiting our ability to enhance a spatial point, and the maximum enhancement decays to Emax=1.

Field-of-View: The field-of-view (FOV) of an optimized image is defined as the maximum diameter of the image where the intensity (of a pixel or bead) is half the optimized intensity. This represents the part of the image where the optimization pattern allows for increased image quality (resolution, SNR). As we image deeper into the rock, the FOV decays to the size of a single speckle grain.

Appendix D

Derivation of Deconvolution Approximations

D.1 Derivation of Modulated OTF

We start with an EDOF system that uses a deformable mirror in the pupil plane to change the focus of the microscope system (Fig. 3·1) over a scan range D, from z=-D/2 to z=+D/2. For static illumination L_0, the intensity on the camera is integrated along the axial direction to produce a projected intensity as a function of position, giving an EDOF image I_0. If we then modulate the intensity by a linear ramp $L(z) = L_0 + mz$ in sync with the focal position z, we obtain an image I_m where an objects below the focal plane (z<0) is dimmer and objects above the focal plane (z>0) are brighter, proportional to their axial position. For a single point source located in the imaging volume, we can obtain the lateral and axial co-ordinates of the source by taking a static and a modulated image, and combining appropriately:

$$\begin{aligned} \vec{x_0} &= \big\{(x_0, y_0) | I_0(x_0, y_0) = \max\big[I_0\big]\big\} \\ h_{z_0}(\vec{x}_0) &= \frac{I_m(\vec{x}_0) - I_0(\vec{x}_0)}{\frac{m}{L_0} I_0(\vec{x}_0)} \end{aligned} \tag{D.1}$$

where $\vec{x}_0$ are the lateral co-ordinates and h_{z_0} is the axial position. $m = \frac{\Delta L}{D}$ is the change in illumination intensity over the scan range. This allows for 3D localization of an isolated particle in only two camera frames.

Equation D.1 provides a good approximation for point sources, but breaks down for extended objects. In order to correctly extract the axial position of a laterally extended sample, we derive an explicit form of the Optical Transfer Function (OTF) for linearly modulated illumination that we can use to deconvolve the images. We start with the spatial-frequency intensity distribution in a given imaging plane in terms of the object:

$$\tilde{I}(\vec{k}_\perp, k_z) = OTF(\vec{k}_\perp, k_z)\tilde{O}(\vec{k}_\perp, k_z) \tag{D.2}$$

where $\tilde{O}(\vec{k}_\perp, k_z)$ is the 3D fourier transform of the object, $\tilde{I}(\vec{k}_\perp, k_z)$ is the 3D fourier transform of the image, and $OTF(\vec{k}_\perp, k_z)$ is the 3D optical transfer function of a diffraction-limited imaging system, given by Frieden (Frieden, 1967). Equation D.2 can be reformulated to obtain the intensity in a given imaging plane by taking a Fourier transform with respect to the axial co-ordinate:

$$\begin{aligned}\tilde{I}(\vec{k}_\perp, z) &= \iint e^{i2\pi k_z(z-z_0)} OTF(\vec{k}_\perp, k_z)\tilde{O}(\vec{k}_\perp, z_0)\mathrm{d}k_z\mathrm{d}z_0 \\ &= \iint \cos[2\pi k_z(z-z_0)] OTF(\vec{k}_\perp, k_z)\tilde{O}(\vec{k}_\perp, z_0)\mathrm{d}k_z\mathrm{d}z_0 \\ &= \int OTF_c(\vec{k}_\perp, z-z_0)\tilde{O}(\vec{k}_\perp, z_0)\mathrm{d}z_0\end{aligned} \tag{D.3}$$

where the complex exponential reduces to a cosine due to the OTF in Eq. D.3 being symmetric in k_z. By modulating the intensity and the imaging plane in-sync using the deformable mirror, we integrate the intensity along the axial co-ordinate to obtain:

$$\tilde{I}_m(\vec{k}_\perp, D) = \int_{-D/2}^{D/2} \frac{\mathrm{d}z}{D} L_m(z) \int OTF_c(\vec{k}_\perp, z-z_0)\tilde{O}(\vec{k}_\perp, z_0)\mathrm{d}z_0 \tag{D.4}$$

where D is the full depth-of-field. $L(z)$ is the illumination modulation given by: $L(z) = L_0 + mz$, where L_0 is the illumination intensity in the nominal focal plane

$(z = 0)$ and $m = \frac{\Delta L}{D}$ is the change in intensity over the scan range. This defines an effective OTF for a specific imaging plane given by:

$$OTF_D(\vec{k}_\perp, z_0) = \int_{-D/2}^{D/2} \frac{\mathrm{d}z}{D} L(z) OTF_c(\vec{k}_\perp, z - z_0) \tag{D.5}$$

Equation D.5 can be explicitly integrated over z to obtain:

$$\begin{aligned} OTF_D(\vec{k}_\perp, z_0) = \int \Big[& L_0 \mathrm{sinc}[2\pi k_z D] \cos[2\pi k_z z_0] \\ & + m z_0 \mathrm{sinc}[2\pi k_z D] \mathrm{sinc}[2\pi k_z z_0] \\ & - m z_0 \cos[2\pi k_z D] \mathrm{sinc}[2\pi k_z z_0] \Big] OTF(\vec{k}_\perp, k_z) \mathrm{d}k_z \end{aligned} \tag{D.6}$$

In the limit of small axial displacement (that is, the object is well within the scan range), we can approximate Eq. D.6 to linear order in z_0, reducing it to:

$$OTF_D(\vec{k}_\perp, z_0) = (L_0 + m z_0) EOTF(\vec{k}_\perp, D) - m z_0 OTF_c(\vec{k}_\perp, D/2) \tag{D.7}$$

Where $EOTF(\vec{k}_\perp, D)$ is the OTF for a uniformly illuminated focal scan resulting in an extended depth of field (Shain et al., 2017b), and $OTF_c(\vec{k}_\perp, D/2)$ is the OTF for an image plane at a depth of D/2 relative to the nominal focal plane. Substituting Eq. D.7 into Eq. D.4 allows us to isolate the average axial position of the sample:

$$\tilde{I}_m(\vec{k}_\perp, D) - \tilde{I}_0(\vec{k}_\perp, D) = m\big[EOTF(\vec{k}_\perp, D) - OTF_c(\vec{k}_\perp, D/2)\big] \int z_0 \tilde{O}(\vec{k}_\perp, z_0) \mathrm{d}z_0 \tag{D.8}$$

where $\tilde{I}_0(\vec{k}_\perp, D) = L_0 EOTF(\vec{k}_\perp, D) \int \tilde{O}(\vec{k}_\perp, z_0) \mathrm{d}z_0$ is the constant illumination extended depth-of-field image. Dividing by the OTF terms gives:

$$\frac{\left[\tilde{I}_m(\vec{k}_\perp, D) - \tilde{I}_0(\vec{k}_\perp, D)\right]}{m\left[EOTF(\vec{k}_\perp, D) - OTF_c(\vec{k}_\perp, D/2)\right]} = \int z_0 \tilde{O}(\vec{k}_\perp, z_0)\mathrm{d}z_0 \tag{D.9}$$

which we can convert to the full real-space co-ordinates by taking an inverse Fourier transform:

$$F^{-1}\left[\frac{\left[\tilde{I}_m(\vec{k}_\perp, D) - \tilde{I}_0(\vec{k}_\perp, D)\right]}{m\left[EOTF(\vec{k}_\perp, D) - OTF_c(\vec{k}_\perp, D/2)\right]}\right] = \int z_0 O(\vec{x}_0, z_0)\mathrm{d}z_0 \tag{D.10}$$

Prompting us to define the modulated $MOTF(\vec{k}_\perp, D) = EOTF(\vec{k}_\perp, D) - OTF_c(\vec{k}_\perp, D/2)$. Similarly, we can obtain the axially-averaged intensity by taking a uniform-illumination scan:

$$F^{-1}\left[\frac{\tilde{I}_0(\vec{k}_\perp, D)}{L_0 EOTF(\vec{k}_\perp, D)}\right] = \int O(\vec{x}_0, z_0)\mathrm{d}z_0 \tag{D.11}$$

For an axially sparse sample, such as a surface, membrane, or isolated particle, the object function separates into lateral and axial components: $O(\vec{x}_0, z_0) = O(\vec{x}_0)\delta(z_0 - h_{z_0}(\vec{x}_0))$. Inserting this into Equations D.10 and D.11 lets us isolate the height of the sample as a function of lateral position:

$$\begin{aligned} O(\vec{x}_0) &= \int O(\vec{x}_0, z_0)\mathrm{d}z_0 \\ h_{z_0}(\vec{x}_0) &= \frac{\int z_0 O(\vec{x}_0, z_0)\mathrm{d}z_0}{\int O(\vec{x}_0, z_0)\mathrm{d}z_0} \end{aligned} \tag{D.12}$$

Which provides a more accurate version of Eq. D.1.

References

Abrahamsson, S., Usawa, S., and Gustafsson, M. (2006). A new approach to extended focus for high-speed, high-resolution biological microscopy. *Proc. SPIE*, 6090:60900N.

Alix-Panabières, C. and Pantel, K. (2013). Circulating tumor cells: Liquid biopsy of cancer. *Clinical Chemistry*, 59(1):110–118.

Archer-Zhang, C. C. C., Foster, W. B., Downey, R. D., Arrasmith, C. L., and Dickensheets, D. L. (2016). Dynamic performance of microelectromechanical systems deformable mirrors for use in an active/adaptive two-photon microscope. *Journal of Biomedical Optics*, 21(12).

Berkovits, R. and Feng, S. (1994). Correlations in coherent multiple scattering. *Physics Reports*, 238(3):135 – 172.

Berlich, R., Bräuer, A., and Stallinga, S. (2016). Single shot approach for three-dimensional imaging with double-helix point spread functions. In *Imaging and Applied Optics 2016*, page CTh1D.4. Optical Society of America.

Bertero, M. and Boccacci, P. (1998). *Introduction to inverse problems in imaging.* IOP Publishing.

Bifano, T. (2010). Shaping light: Moems deformable mirrors for microscopes and telescopes.

Bishara, W., Sikora, U., Mudanyali, O., Su, T.-W., Yaglidere, O., Luckhart, S., and Ozcan, A. (2011). Holographic pixel super-resolution in portable lensless on-chip microscopy using a fiber-optic array. *Lab Chip*, 11:1276–1279.

Blasi, T., Hennig, H., Summers, H. D., Theis, F. J., Cerveira, J., Patterson, J. O., Davies, D., Filby, A., Carpenter, A. E., and Rees, P. (2016). Label-free cell cycle analysis for high-throughput imaging flow cytometry. *Nature Communications*, 7:10256.

Booth, M. J. (2014). Adaptive optical microscopy: the ongoing quest for a perfect image. *Light: Science & Applications*, 3(4):e165.

Carter, C. D., Hammack, S., and Lee, T. (2016). High-speed flamefront imaging in premixed turbulent flames using planar laser-induced fluorescence of the CH C-X band. *Combustion and Flame*, 168:66–74.

Chambolle, A. and Pock, T. (2016). An introduction to continuous optimization for imaging. *Acta Numerica*, 25:161319.

Chen, T. H., Ault, J. T., Stone, H. A., and Arnold, C. B. (2017). High-speed axial-scanning wide-field microscopy for volumetric particle tracking velocimetry. *Experiments in Fluids*, 58(41):1–7.

Christie, I. N., Wells, J. A., Kasparov, S., Gourine, A. V., and Lythgoe, M. F. (2017). Volumetric Spatial Correlations of Neurovascular Coupling Studied using Single Pulse Opto-fMRI. *Scientific Reports*, 7:41583.

Constantino, M. A., Jabbarzadeh, M., Fu, H. C., and Bansil, R. (2016). Helical and rod-shaped bacteria swim in helical trajectories with little additional propulsion from helical shape. *Scientific Advances*, 2:e1601661–e1601661–14.

Copeland, M., Price, I., Rigaut, F., Bloxham, G., Boz, R., Bundy, D., Espeland, B., and Sharp, R. (2016). Gmtifs: deformable mirror environmental testing for the on-instrument wavefront sensor.

Crosignani, V., Dvornikov, A. S., Aguilar, J. S., Stringari, C., Edwards, R. A., Mantulin, W. W., and Gratton, E. (2012). Deep tissue fluorescence imaging and in vivo biological applications. *Journal of Biomedical Optics*, 17:17 – 17 – 7.

Datta, S. S., Chiang, H., Ramakrishnan, T. S., and Weitz, D. A. (2013). Spatial fluctuations of fluid velocities in flow through a three-dimensional porous medium. *Phys. Rev. Lett.*, 111:064501.

Dowski, E. R. and Cathey, W. T. (1995). Extended depth of field through wave-front coding. *Applied Optics*, 34(11):1859–1866.

Dufour, P., Piché, M., De Koninck, Y., and McCarthy, N. (2006). Two-photon excitation fluorescence microscopy with a high depth of field using an axicon. *Applied Optics*, 45:9246–9252.

Fredrich, J. T., DiGiovanni, A. A., and Noble, D. R. (2006). Predicting macroscopic transport properties using microscopic image data. *Journal of Geophysical Research: Solid Earth*, 111(B3):n/a–n/a. B03201.

Frentz, Z., Kuehn, S., Hekstra, D., and Leibler, S. (2010). Microbial population dynamics by digital in-line holographic microscopy. *Rev. Sci. Instrum.*, 81:084301.

Frieden, B. (1967). Optical Transfer of the Three-Dimensional Object. *J. Opt. Soc. Am.*, 57:56–66.

Futamura, K., Sekino, M., Hata, A., Ikebuchi, R., Nakanishi, Y., Egawa, G., Kabashima, K., Watanabe, T., Furuki, M., and Tomura, M. (2015). Novel full-spectral flow cytometry with multiple spectrally-adjacent fluorescent proteins and fluorochromes and visualization of in vivo cellular movement. *Cytometry Part A*, 87(9):830–842.

Genack, A. Z. (1987). Optical Transmission in Disordered Media. *Phys. Rev. Lett*, 58(20):2043–2046.

Giese, J. D., Ford, T., and Mertz, J. (2014). Fast volumetric phase-gradient imaging in thick samples. *Optics Express*, 22:1152–1162.

Gong, Y., Huang, C., Li, J. Z. Z., Grewe, B. F., Zhang, Y., Eismann, S., and Schnitzer, M. J. (2015). High-speed recording of neural spikes in awake mice and flies with a fluorescent voltage sensor. *Science*, 350(6266):1361–1366.

Goodman, J. W. (2007). *Speckle Phenomena in Optics.* Roberts and Company, Greenwood Village, CO.

Grewe, B. F., Voigt, F. F., van 't Hoff, M., and Helmchen, F. (2011). Fast two-layer two-photon imaging of neuronal cell populations using an electrically tunable lens. *Biomedical Optics Express*, 2(7):2035–2046.

Hausler, G. (1972). A method to increase the depth of focus by two step image processing. *Optics Communications*, 6(1):38–42.

Indebetouw, G. and Bai, H. (1984). Imaging with Fresnel zone pupil masks: extended depth of field. *Applied Optics*, 23(23):4299–4302.

Inglis, A., Cruz, L., Roe, D. L., Stanley, H. E., Rosene, D. L., and Urbanc, B. (2008). Automated identification of neurons and their locations. *Journal of Microscopy*, 230(3):339–352.

Ishimaru, A. (1978). *Wave Propagation and Scattering in Random Media.* Academic Press, New York, NY.

Jackson, J. D. (1999). *Classical electrodynamics.* Wiley, New York, NY, 3rd ed. edition.

Ji, N. (2014). The practical and fundamental limits of optical imaging in mammalian brains. *Neuron*, 83(6):1242–1245.

Ji, N., Freeman, J., and Smith, S. L. (2016). Technologies for imaging neural activity in large volumes. *Nature Neuroscience*, 19(9):1154–1164.

Jost, A., Tolstik, E., Feldmann, P., Wicker, K., Sentenac, A., and Heintzmann, R. (2015). Optical sectioning and high resolution in single-slice structured illumination microscopy by thick slice blind-sim reconstruction. *PLOS ONE*, 10(7):1–10.

Judkewitz, B., Horstmeyer, R., Vellekoop, I. M., Papadopoulos, I. N., and Yang, C. (2015). Translation correlations in anisotropically scattering media. *Nature Physics*, 11:684–689.

Katz, O., Heidmann, P., Fink, M., and Gigan, S. (2014). Non-invasive single-shot imaging through scattering layers and around corners via speckle correlations. *Nature Photonics*, 8:784–790.

Lei, C., Ito, T., Ugawa, M., Nozawa, T., Iwata, O., Maki, M., Okada, G., Kobayashi, H., Sun, X., Tiamsak, P., Tsumura, N., Suzuki, K., Carlo, D. D., Ozeki, Y., and Goda, K. (2016). High-throughput label-free image cytometry and image-based classification of live euglena gracilis. *Biomed. Opt. Express*, 7(7):2703–2708.

Leme, D. M., Grummt, T., de Oliveira, D. P., Sehr, A., Renz, S., Reinel, S., Ferraz, E. R. A., de Marchi, M. R. R., Machado, M. C., Zocolo, G. J., and Marin-Morales, M. A. (2012). Genotoxicity assessment of water soluble fractions of biodiesel and its diesel blends using the salmonella assay and the in vitro microflow kit (litron) assay. *Chemosphere*, 86(5):512 – 520.

Li, J., Beaulieu, D. R., Paudel, H., Barankov, R., Bifano, T. G., and Mertz, J. (2015). Conjugate adaptive optics in widefield microscopy with an extended-source wavefront sensor. *Optica*, 2(8):682–688.

Lin, H. W., Tegmark, M., and Rolnick, D. (2017). Why does deep and cheap learning work so well? *Journal of Statistical Physics*, 168(6):1223–1247.

Llull, P., Yuan, X., Carin, L., and Brady, D. J. (2015). Image translation for single-shot focal tomography. *Optica*, 2(9):822–825.

Lu, R., Sun, W., Liang, Y., Kerlin, A., Bierfeld, J., Seelig, J. D., Wilson, D. E., Scholl, B., Mohar, B., Tanimoto, M., Koyama, M., Fitzpatrick, D., Orger, M. B., and Ji, N. (2017). Video-rate volumetric functional imaging of the brain at synaptic resolution. *Nat. Neurosci.*, 20:620–628.

Lu, S.-H. and Hua, H. (2015). Imaging properties of extended depth of field microscopy through single-shot focus scanning. *Optics Express*, 23:10714–10731.

Mathaes, R., Hildebrandt, C., Winter, G., Engert, J., and Besheer, A. (2013). Quality control of protein crystal suspensions using microflow imaging and flow cytometry. *Journal of Pharmaceutical Sciences*, 102(10):3860 – 3866.

Maurer, C., Jesacher, A., Bernet, S., and Ritsch-Marte, M. (2011). What spatial light modulators can do for optical microscopy. *Laser & Photonics Reviews*, 5(1):81–101.

Meitav, N., Ribak, E. N., and Shoham, S. (2016). Point spread function estimation from projected speckle illumination. *Light: Science & Applications*, 5:e16048.

Memmolo, P., Miccio, L., Paturzo, M., DiCaprio, G., Coppola, G., Netti, P. A., and Ferraro, P. (2015). Recent advances in holgraphic 3D particle tracking. *Adv. Opt. Photon.*, 7:713–755.

Mertz, J. (2010). *Introduction to Optical Microscopy.* Roberts and Company, Greenwood Village, CO, 2nd ed. edition.

Pasternack, R. M., Qian, Z., Zheng, J.-Y., Metaxas, D. N., White, E., and Boustany, N. N. (2008). Measurement of subcellular texture by optical gabor-like filtering with a digital micromirror device. *Opt. Lett.*, 33(19):2209–2211.

Paudel, H. P. (2015). *Coherent beam control through inhomogeneous media in multiphoton microscopy.* PhD thesis. Copyright - Database copyright ProQuest LLC; ProQuest does not claim copyright in the individual underlying works; Last updated - 2016-06-06.

Paudel, H. P., Stockbridge, C., Mertz, J., and Bifano, T. (2013). Focusing polychromatic light through strongly scattering media. *Optics Express*, 21(14):17299–17308.

SHAH, S., CRAWSHAW, J., and BOEK, E. (2017). Three-dimensional imaging of porous media using confocal laser scanning microscopy. *Journal of Microscopy*, 265(2):261–271.

Shain, W., Paudel, H., Eichmann, S. L., Kanj, M., Bifano, T., and Goldberg, B. (2015). Adaptive multi-photon imaging of subsurface nanoparticle flow in porous rock. In *Imaging and Applied Optics 2015*, page AOM4B.5. Optical Society of America.

Shain, W. J., Goldberg, B. B., Bifano, T., and Mertz, J. (2017a). Matched-filter compressive imaging using a deformable mirror for label-free flow cytometry. In *Imaging Systems and Applications*, pages ITu4E–1. Optical Society of America.

Shain, W. J., Vickers, N. A., Goldberg, B. B., Bifano, T., and Mertz, J. (2017b). Extended depth-of-field microscopy with a high-speed deformable mirror. *Opt. Lett.*, 42(5):995–998.

Shain, W. J., Vickers, N. A., Negash, A., Bifano, T., Sentenac, A., and Mertz, J. (2017c). Dual fluorescence-absorption deconvolution applied to extended-depth-of-field microscopy. *Opt. Lett.*, 42(20):4183–4186.

Sinha, A., Lee, J., Li, S., and Barbastathis, G. (2017). Lensless computational imaging through deep learning. *Optica*, 4(9):1117–1125.

Smith, M. L., Chyla, B., McKeegan, E., and Tahir, S. K. (2016). Development of a flow cytometric method for quantification of bcl-2 family members in chronic lymphocytic leukemia and correlation with sensitivity to bcl-2 family inhibitors. *Cytometry Part B: Clinical Cytometry*, 92(5):331–339.

Steinvall, O., Berglund, F., Allard, L., and Berggren, J. (2017). Imaging and laser profiling for airborne target classification.

Stockbridge, C., Lu, Y., Moore, J., Hoffman, S., Paxman, R., Toussaint, K., and Bifano, T. (2012). Focusing through dynamic scattering media. *Opt. Express*, 20(14):15086–15092.

Tang, J., Germain, R. N., and Cui, M. (2012). Superpenetration optical microscopy by iterative multiphoton adaptive compensation technique. *Proceedings of the National Academy of Sciences*, 109(22):8434–8439.

Theis, L., Berens, P., Froudarakis, E., Reimer, J., RomnRosn, M., Baden, T., Euler, T., Tolias, A., and Bethge, M. (2016). Benchmarking spike rate inference in population calcium imaging. *Neuron*, 90(3):471 – 482.

Thomas, S. (2008). Enhanced oil recovery - an overview. *Oil & Gas Science and Technology - Rev. IFP*, 63(1):9–19.

Vellekoop, I. M. and Mosk, A. P. (2007). Focusing coherent light through opaque strongly scattering media. *Opt. Lett.*, 32(16):2309–2311.

Wang, A., Garmann, R. F., and Manoharan, V. N. (1960). Tracking E. coli runs and tumbles with scattering solutions and digital holographic microscopy. *Optics Express*, 50(21):23719–23725.

Welford, W. T. (1960). Use of Annular Apertures to Increase Focal Depth. *J. Opt. Soc. Am.*, 50(8):749–753.

Wojcik, K. and Dobrucki, J. W. (2008). Interaction of a dna intercalator draq5, and a minor groove binder syto17, with chromatin in live cellsinfluence on chromatin organization and histonedna interactions. *Cytometry Part A*, 73A(6):555–562.

Yang, W., Miller, J.-e. K., Carrillo-Reid, L., Pnevmatikakis, E., Paninski, L., Yuste, R., and Peterka, D. S. (2016). Simultaneous multi-plane imaging of neural circuits. *Neuron*, 89(2):269–284.

Yang, W. and Yuste, R. (2017). In vivo imaging of neural activity. *Nature Methods*, 14(4):349–359.

Youssef, S. (1987). Clustering with local equivalence relations. *Computer Physics Communications*, 45(1):423 – 426.

Yu, H., Hillman, T. R., Choi, W., Lee, J. O., Feld, M. S., Dasari, R. R., and Park, Y. (2013). Measuring large optical transmission matrices of disordered media. *Phys. Rev. Lett.*, 111:153902.

Zhou, J., Cao, Z., Xie, H., and Xu, L. (2015). Digital micro-mirror device-based detector for particle-sizing instruments via fraunhofer diffraction. *Appl. Opt.*, 54(18):5842–5849.

Zhuang, J. and Sitti, M. (2016). Chemotaxis of bio-hybrid multiple bacteria-driven microswimmers. *Scientific Reports*, 6:32135–32135–14.

Curriculum Vitae

[redacted]

[redacted]

[redacted]